Multi-elemental Statistical Features of Early Paleogene Sediments from the Mid-latitude Eastern Indian Ocean

Yusuke Kuwahara[1,2], Kazutaka Yasukawa[3,1], Erika Tanaka[4,3], Kentaro Nakamura[3,1,2], Minoru Ikehara[4], and Yasuhiro Kato[1,2]

[1]Department of Systems Innovation, School of Engineering, The University of Tokyo, 7-3-1 Hongo, Bunkyo-ku, Tokyo, 113-8656, Japan.

[2]Ocean Resources Research Center for Next Generation, Chiba Institute of Technology, 2-17-1 Tsudanuma, Narashino, Chiba, 275-0016, Japan.

[3]Frontier Research Center for Energy and Resources, School of Engineering, The University of Tokyo, 7-3-1 Hongo, Bunkyo-ku, Tokyo, 113-8656, Japan.

[4]Marine Core Research Institute, Kochi University, 200 Monobe Otsu, Nankoku, Kochi, 783-8502, Japan.

Corresponding author: Yasuhiro Kato (ykato@sys.t.u-tokyo.ac.jp) ORCID: 0000-0002-5711-8304

Key Points:

- Here, we report bulk $\delta^{13}C$, $\delta^{18}O$, and chemical compositions of early Paleogene sediments from Site 762C in the Indian Ocean.
- We conducted independent component analysis on the bulk chemical composition to evaluate the geochemistry of the depositional area.
- Environmental factors including terrigenous input, productivity, and redox at the site changed during early Paleogene hyperthermals.

Abstract

The early Paleogene is characterized by a "hothouse" environment with repetitive transient warming events known as "hyperthermals." While these paleoenvironmental changes are well-documented in the Pacific and Atlantic Oceans, records of such changes in the Indian Ocean are limited. Here, we present a new dataset of bulk chemical composition and stable isotopic ratios of the late Paleocene–middle Eocene sediments on the Exmouth Plateau in the mid-latitude eastern Indian Ocean. The bulk $\delta^{13}C$ and $\delta^{18}O$ suggest a warming period called the Early Eocene Climate Optimum (EECO) and cooling towards the middle Eocene in a long-term perspective. From a short-term perspective, we identified at least five hyperthermals (PETM, H2, I1, J, and ETM3) in the studied sections. We identified six independent components (ICs) corresponding to sediment source materials and post-depositional processes by applying independent component analyses (ICA) to the bulk chemical composition data. The time-series behavior of IC3 indicates an increase in detrital material or a decrease in carbonate rain flux during both long-term (EECO) and short-term (hyperthermal) warming. Additionally, the rise in IC2 implies an increased population of high consumers in the oceanic ecosystem during warming events around the Exmouth Plateau. Other ICs (IC1, IC4, IC5, and IC6), indicators of diagenetic processes and post-depositional remobilization of elements, showed excursions across hyperthermal horizons. These observations indicate that changes in the redox state of pore or bottom water in the Exmouth Plateau are associated with hyperthermals.

1 Introduction

Among the long-term climatic trends of the Cenozoic, the early Paleogene is a globally warm period. In the long-term (~ 10^6 yr) climatic trend, the global climate has been warmer since the Paleocene, and the peak of the warming is called the Early Eocene Climate Optimum (EECO, 53.260–49.140 Ma; Westerhold et al., 2020; Zachos et al., 2001). After EECO, the climate trend turned to long-term cooling towards the middle Eocene. Superimposed on the million-years-long warm period during the late Paleocene–early Eocene are well-known transient (10^4–10^5 yr) warming events called "hyperthermals" (e.g., Thomas, 1998; Westerhold et al., 2018). In particular, the Paleocene–Eocene Thermal Maximum (PETM, 56 Ma) is the most pronounced and well-studied hyperthermal event, characterized by intense global warming (5–9 °C rise in sea surface temperature: SST) and ocean acidification associated with the negative carbon isotope ($\delta^{13}C$) excursion (CIE, e.g., Kennett & Stott, 1991; McInerney & Wing, 2011; Zachos et al., 2003, 2005). In addition to the PETM, many hyperthermals accompanying negative CIEs, such as the Eocene Thermal Maximum 2 (ETM2), H2, I1, I2, J, and ETM3, have been reported. The background climate, referred to as a "hothouse" climate, and hyperthermals during the early Paleogene have garnered considerable attention as a paleo-analog to the potential fate of contemporary climate changes, including global warming.

The paleoceanographic environment during the early Paleogene has been deduced from geochemical records of seafloor sediments. One characteristic paleoceanographic change associated with warming is carbonate compensation depth (CCD) elevation. From a long-term perspective (~10^6 yr), the CCD shallowed during the EECO (Pälike et al., 2012); however, from a short-term perspective (~10^5 yr), CCD shallowing also occurred in hyperthermals (e.g., Raffi & Bernardi, 2008; Slotnick et al., 2015: Zachos et al., 2005). The CCD shallowing corresponding to the long- and short-term warming has been attributed to the pH lowering of seawater due to high atmospheric pCO_2 (e.g., Anagnostou et al., 2016, 2020; Pälike et al., 2012; Zachos et al., 2005).

The ocean stratification, acidification, and deep-water deoxygenation at hyperthermals, particularly in the PETM, have also been inferred by foraminiferal records (e.g., Kaiho et al., 2006; Thomas, 1998) and the enrichment/depletion of redox-sensitive-elements in the marine sediments (Chun et al., 2010; Pälike et al., 2014).

The Indian Ocean, the major seawater path between the Atlantic and the Pacific during the early Paleogene (Thomas et al., 2003), is important in elucidating paleoceanographic conditions during the early Paleogene in a global context. Geochemical investigation of Indian Ocean sediments can provide fundamental keys for evaluating global behavior in the early Paleogene hothouse. While geochemical records of hyperthermals, especially of the PETM, from the Atlantic and Pacific Oceans have been well established (e.g., Cramer et al., 2003; Hollis et al., 2015; Lauretano et al., 2015; Leon-Rodriguez & Dickens, 2010; Littler et al., 2014; Lourens et al., 2005; Stap et al., 2010; Westerhold et al., 2018), there are only a few records of hyperthermals from the Indian Ocean (Slotnick et al., 2015; Tanaka et al., 2022; Tremolada & Bralower, 2004; Yasukawa et al., 2017).

In this context, we focused on the Ocean Drilling Program (ODP) Site 762 Hole C from offshore of the northwestern margin of the Australian continent (Exmouth Plateau; Figure 1a). The ODP results reported bulk carbonate $\delta^{13}C$ and $\delta^{18}O$ records from Site 762C (Thomas et al., 1992) and roughly indicate the existence of multiple hyperthermals supported by paleomagnetic and biostratigraphic studies (Galbrun, 1992; Shamrock & Watkins, 2012; Shamrock et al., 2012). However, the temporal resolution of the reported $\delta^{13}C$ and $\delta^{18}O$ records was low, and hyperthermal horizons were not firmly determined. Here, we report higher resolution records of bulk $\delta^{13}C$ and $\delta^{18}O$ from the early Paleogene (late Paleocene–middle Eocene) section of Site 762C, identify hyperthermal horizons, and show long-term $\delta^{13}C$ and $\delta^{18}O$ trends at the site. Further, based on the bulk $\delta^{13}C$ record, we revised the age model of Site 762C core.

In addition to the C and O isotopes, we analyzed the bulk chemical composition of the early Paleogene carbonate sediments of Site 762C to discuss the paleoceanographic condition at the site in the Eocene. The bulk chemical composition of seafloor sediments reflects the mixed signals of each source material and post-depositional element redistribution (e.g., Dunlea et al., 2015; Plank & Langumuir, 1998). However, applying conventional approaches based on the bivariate correlations among each element or normalized data is difficult when extracting and interpreting essential information from multi-element datasets. In particular, carbonate sediments are challenging to decipher source materials and post-depositional processes due to the strong dilution effect of biogenic $CaCO_3$ (e.g., Yasukawa et al., 2017). Thus, most previous studies on geochemical features use only representative elements' abundances, which inevitably exclude signatures underlying the high-dimensional, entire data structure. To overcome these challenges, we applied multivariate statistical analysis to extract geochemical signals hidden in multi-elemental data of the bulk-chemical composition of Site 762C sediments.

Multivariate statistical analyses have been utilized for interpreting geochemical data (e.g., Dunlea et al., 2015; Iwamori & Albarède, 2008; Kato et al., 2011; Yasukawa et al., 2016, 2017, 2019, 2022). As the bulk elemental composition of seafloor sediments reflects an admixture of multiple source materials and geochemical processes (e.g., diagenesis, redistribution, precipitation), multivariate statistical analysis is considered a powerful approach for extracting geochemical signals hidden in the high-dimensional data structure. Among various analytic methods, independent component analysis (ICA) extracts features based on non-Gaussianity in a multivariate dataset and is considered an appropriate analytical method for geochemical data

with a non-Gaussian data structure (e.g., Iwamori & Albarède, 2008; Yasukawa et al., 2016, 2017). In recent years, ICA has been successfully applied to high-dimensional geochemical datasets, including the bulk chemical composition of seafloor sediments (Kato et al., 2011; Yasukawa et al., 2016, 2017, 2019). By applying ICA, the observed multidimensional dataset consisting of the concentration of each element could be transformed into the linear combination of base vectors (independent components: ICs) corresponding to the source materials and geochemical processes of the sediments. For detailed formulation on using ICA in marine sediment analysis, see Yasukawa et al. (2016). In this study, by applying ICA to the geochemical dataset, we evaluated the paleoceanographic changes at Site 762C in the mid-latitude eastern Indian Ocean.

2 Geological Settings and Lithology

ODP Leg 122 Site 762 Hole C (19°53.23S, 112°15.24E) is located on the central Exmouth Plateau in the Northern Carnarvon Basin, where ~300 km offshore of the northwestern coast of the Australian continent. According to the paleogeographic reconstruction (Scotese, 2001), the Exmouth plateau was located in the mid-latitude of the eastern margin of the Indian Ocean during the early Paleogene (~60–40 Ma; Figure 1a). The Northern Carnarvon Basin was initially formed by the stretching during Carboniferous–Cretaceous, and the Exmouth plateau has been thought to be inactive after mid-Cretaceous. Since then, the Cenozoic sedimentary environment has corresponded to an open-ocean setting (Bilal & McClay, 2022; Haq et al., 1992). The present-day water depth of this site is 1360 m (Haq et al., 1990; Figure 1b), and the paleodepth of the early Paleogene is comparable to that reported today (1000–1200 m; Haq et al., 1992; Jones & Wonders, 1992).

The lithology of the early Paleogene section of Site 762C mainly consists of nannofossil chalk that was deposited above the CCD and has been divided into three lithologic subunits (Unit II, Subunit IIIA, and Subunit IIIB; Haq et al., 1990; Shamrock et al., 2012). Unit II (181.5–265.0 mbsf: meter(s) below seafloor) consists of white consolidated nannofossil ooze/chalk deposited during the middle Eocene to the early Oligocene. Subunit IIIA (265.0–398.0 mbsf) consists of pale green–light green-grey nannofossil chalk with foraminifers deposited during the early–middle Eocene. Subunit IIIB (398.0–554.8 mbsf) consists of light green-grey–white nannofossil chalk deposited during the early Paleocene–early Eocene. Previous studies based on magnetostratigraphy and biostratigraphy identified four hiatuses in the early Paleogene section of Site 762C (Hiatus A: 289.75 mbsf, Hiatus B: 321.13 mbsf, Hiatus C: 332.18 mbsf, Hiatus D: 412.75 mbsf; Shamrock et al., 2012).

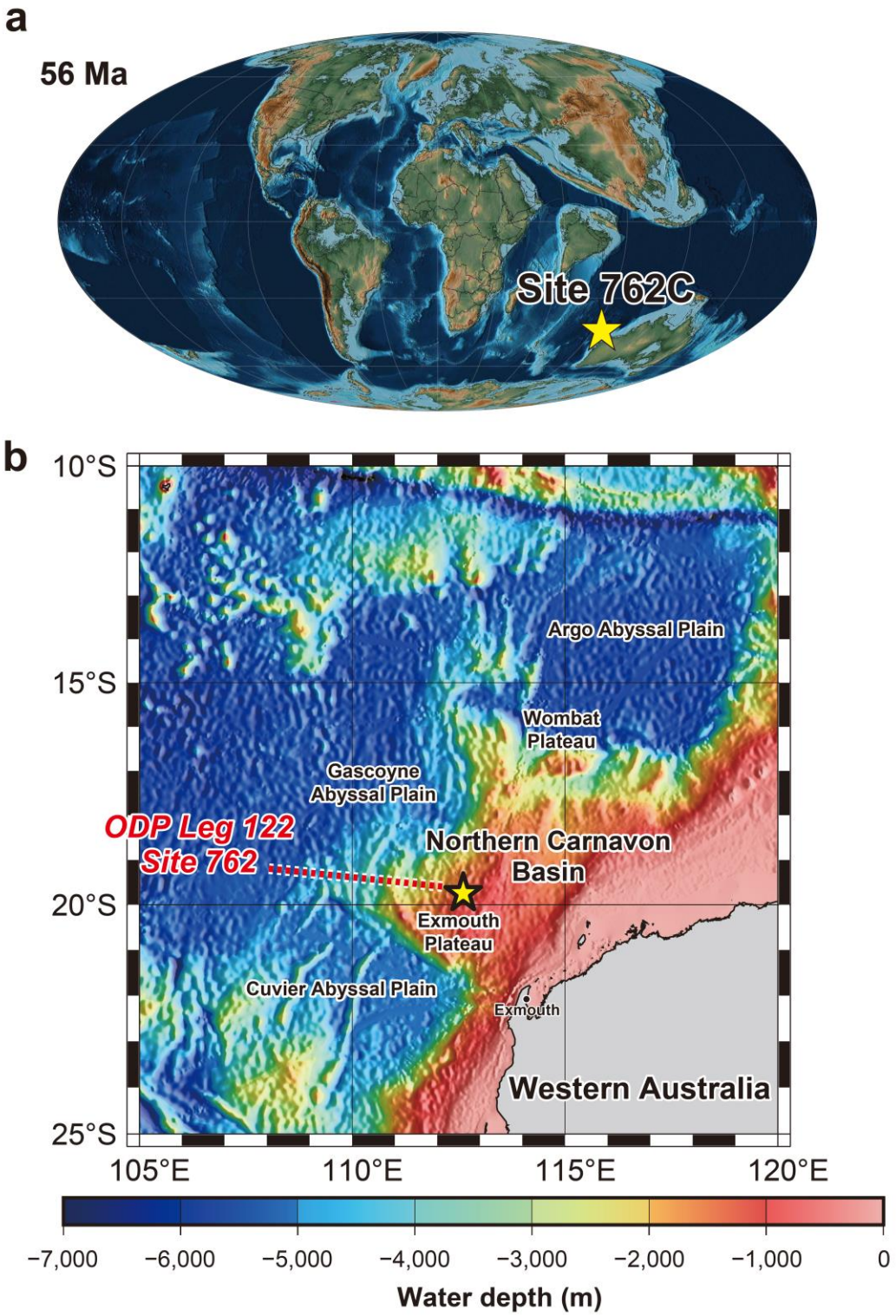

Figure 1. Location of studied site. (a) Paleogeographic reconstruction at the latest Paleocene (56 Ma) using data by Scotese (2001). Stars indicate the paleo-location of ODP Site 762C. (b) Current location of the Exmouth Plateau and ODP Site 762C. The bathymetry is based on 1 min gridded relief data by NOAA (ETOPO1; https://www.ngdc.noaa.gov/mgg/global/global.html).

3 Materials and Methods

3.1 Materials

We targeted 248 samples from the late Paleocene (Thanetian)–middle Eocene (Bartonian) section of Site 762C, corresponding to lithologic Subunits IIIA and IIIB. The sampling resolution was 5–50 kyr for the latest Paleocene–early Eocene section, which was considered to record the PETM and early Eocene hyperthermals. We collected samples with >50 kyr intervals from other sections. All samples were collected from the working half, and the consolidated mud slurry between "biscuits" of actual sediments was carefully avoided.

As a result of the smear slide observations, obtained samples of Site 762C mainly consist of calcareous nannofossil, which can be considered as fragments of coccolith (70–95%) and planktonic foraminiferal shells (2–30%). The contribution of detrital components (e.g., quartz, feldspar, clay minerals) was minor (<5%). In addition, authigenic pyrite grains (100–200 μm) were observed at Core 28X (412.86–413.36 mbsf).

3.2 Carbon and Oxygen Stable Isotope Analyses

Before the geochemical analyses, bulk samples were dried in a vacuum freeze dryer (EYELA FDU-1200) and crushed by an agate mortar and pestle. After sample preparation, we conducted carbon ($\delta^{13}C$) and oxygen ($\delta^{18}O$) stable isotope analyses using GV Instruments IsoPrime with a dual-inlet system at the Center for Advanced Marine Core Research (present Marine Core Research Institute), Kochi University. Approximately 100 μg of pulverized bulk samples were dissolved in phosphoric acid at 90 °C, and released CO_2 was injected into the mass spectrometer.

The measured isotopic ratios were converted from standard delta notation to Vienna Pee Dee Belemnite by analyzing IAEA-603 standard reference material ($\delta^{13}C$ = 2.460 ± 0.010‰, $\delta^{18}O$ = –2.370 ± 0.040‰; Assonov et al., 2020). We also measured $\delta^{13}C$ and $\delta^{18}O$ of geological reference carbonate materials (JCp-1) by the Geological Survey of Japan (GSJ) to evaluate analytical precision. In repeated analyses of IAEA-603 (n = 60) and JCp-1 (n = 7), the 2SE of $\delta^{13}C$ and $\delta^{18}O$ were less than ±0.02‰ and ±0.04‰, respectively.

3.3 Bulk Carbonate Analyses

The bulk carbonate content was determined using an elemental analyzer (Thermo Finnigan EA1112) installed at the Center for Advanced Marine Core Research (present Marine Core Research Institute), Kochi University. In this analysis, we assumed that the total inorganic carbon (TIC) of each sediment sample was incorporated as $CaCO_3$, and TIC corresponds to the difference between total carbon (TC) and total organic carbon (TOC) contents. Therefore, we obtained bulk $CaCO_3$ content (wt.%) using the following equations:

$$[\mathrm{TIC}] = [\mathrm{TC}] - [\mathrm{TOC}] \quad (1)$$

$$[\mathrm{CaCO_3}] = [\mathrm{TIC}] \times \frac{W_{\mathrm{CaCO3}}}{W_c} \quad (2)$$

where W_{CaCO3} and W_C in equation (2) are the formula weight of $CaCO_3$ (100.0869) and the atomic weight of carbon (12.0107), respectively.

In the TC measurement, ~2 mg of bulk samples enclosed in tin capsules were introduced to the elemental analyzer and measured by a packed column. In TOC measurement, ~10 mg of bulk samples were digested by 100 μL of organic-free 3N HCl in silver capsules to remove $CaCO_3$. After drying, the residues of the samples in silver capsules were overwrapped by tin capsules and introduced to the elemental analyzer. To make calibration curves, we simultaneously analyzed sulfanilamide standard reference materials.

3.4 Major- and Trace-element Analyses

The major- and trace-element content of bulk samples was determined by Thermo Fisher Scientific iCAP Q, an inductively coupled plasma quadrupole mass spectrometer (ICP-QMS) installed at the Department of Systems Innovation, School of Engineering, the University of Tokyo. Each sample was digested by $HF–HNO_3–HClO_4$ and aqua regia, following the established method described by Kato et al. (2005) and Yasukawa et al. (2020). Geological reference materials (JB-2, JB-3, and JMS-2) by GSJ were also prepared simultaneously to evaluate analytical accuracy.

In the ICP-QMS analyses, the difference between analyzed and published data of GSJ standards generally falls within 5%, except for Cr, As, and Ta (Supporting Table S1; Imai et al., 1995; Lu et al., 2007; Makishima & Nakamura, 2006; Yasukawa et al., 2020). The reproductivity of replicate analyses (n = 8) is basically within 5% relative standard deviation (RSD), except for As, Sb, and Ta, which sometimes result in larger than 20% RSD (Supporting Table S1).

3.5 ICA

In this study, we applied ICA to a 248 × 40 data matrix from Site 762C; the rows corresponded to the individual bulk sediment samples, and the columns corresponded to the elements. The variables consist of the abundance of Mg, Al, P, K, Sc, Ti, V, Mn, Fe, Co, Ni, Cu, Zn, Rb, Sr, Y, Zr, Nb, Mo, Cs, Ba, La, Ce, Pr, Nd, Sm, Eu, Gd, Tb, Dy, Ho, Er, Tm, Yb, Lu, Hf, Pb, Th, U, and $CaCO_3$. Sodium content was not included in the matrix because saline could largely affect Na content (Yasukawa et al., 2016). Contents of Cr, As, Sb, and Ta were not included in the ICA because these elements show large RSDs through the analytical batches and large differences (>20%) from published data for standard materials. Before calculation, the dataset was standardized for each element. The computation of the ICA for our dataset was implemented using the open R package “FastICA” originally released by Marchini et al. (2013), with some modifications by Yasukawa et al. (2016, 2023).

In performing ICA, we determined the number of ICs and applied the “Guttman–Kaiser criterion (Guttman, 1954; Kaiser, 1960)” to the eigenvalues obtained from the Principal Component Analysis (PCA) algorithm (Supporting Text S1). Our analysis revealed that the eigenvalues of the first six principal components (PCs 1–6) were greater than unity, and these six components accounted for 87.9% of the total sample variance (Supporting Figure S1; Table S2).

After performing ICA, the results were interpreted based on the relative (i.e., variance-normalized) IC loadings and IC scores. The relative IC loadings denote the contributions of each element to the individual ICs. A large loading indicates a strong correlation between the element concentration and the respective IC. As another output of ICA, the IC score represents the coordinate values of sample data projected into the linear space spanned by IC vectors. In simpler terms, IC scores quantify the intensities of each independent source signal in each sample.

4 Results

4.1 Carbon and Oxygen Stable Isotope Ratios

The analytical data of bulk carbonate $\delta^{13}C$ and $\delta^{18}O$ of Site 762C samples are shown in Supporting Table S3. Depth profiles of $\delta^{13}C$ and $\delta^{18}O$ at Site 762C are shown in Figure 2. In the overall trend from Core 29X to Core 12X, bulk $\delta^{13}C$ values were ~3‰ during 425–413 mbsf and dropped to ~2‰ at ~413 mbsf. Thereafter, the $\delta^{13}C$ gradually decreased to $\delta^{13}C$ = ~0–1‰ from 395 to 340 mbsf. The bulk $\delta^{18}O$ generally started around –1.0‰ between 425 and 340 mbsf and increased to 0.0‰ during 340–307 mbsf. Afterward, bulk $\delta^{18}O$ rose gradually at depths shallower than 280 mbsf and reached ~0.5‰ at 265 mbsf.

We found at least four distinct negative excursions of the bulk $\delta^{13}C$ in Core 25X–23X (Figure 3b). In these cores, bulk $\delta^{18}O$ also shows negative excursions associated with those of $\delta^{13}C$, although the $\delta^{18}O$ fluctuates throughout the section. The magnitude of the four excursions of $\delta^{13}C$ (difference between excursion peak and onset) at 395, 390, 379, and 373 mbsf are –0.6‰, –0.7‰, –0.5‰, and –0.9‰, respectively. Conversely, the magnitudes of $\delta^{18}O$ excursions at each horizon are –0.5‰, –0.2‰, –0.3‰, and –0.4‰, respectively. In addition, several smaller-scale negative excursions of $\delta^{13}C$ (~ –0.4‰) and $\delta^{18}O$ (~ –0.2‰) are also observed in Core 22X–18X (Figure 2a). In contrast, no noticeable negative $\delta^{13}C$ excursion was observed in Core 14X–12X, corresponding to the middle Eocene period.

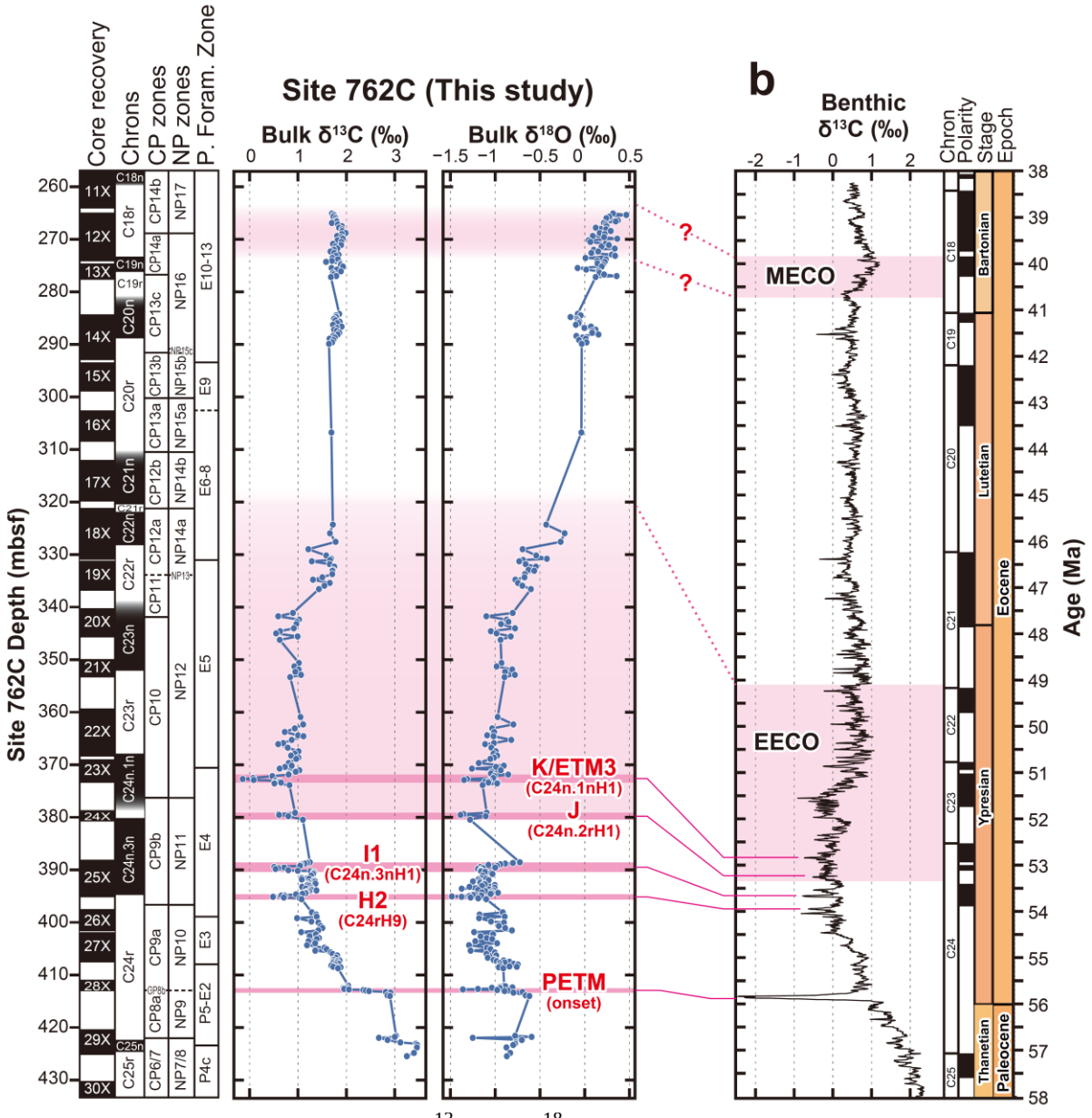

Figure 2. Correlation between (a) bulk $\delta^{13}C$ and $\delta^{18}O$ data from ODP Site 762C and (b) the reference benthic $\delta^{13}C$ profile (Westerhold et al., 2020). Magnetostratigraphy (Galbrun, 1992; Shamrock et al., 2012), calcareous nannofossil (CP zone; Okada & Bukry, 1980, NP zone; Martini, 1971), and planktonic foraminifera biostratigraphy (Hancock et al., 2002; Wade et al., 2011) are also shown in panel (a). Negative carbon isotope excursions of the hyperthermal events with red characters are used as age tie-points. The previously inferred Early Eocene Climate Optimum (EECO) and Middle Eocene Climate Optimum (MECO) are also shown (Shamrock et al., 2012), although we could not identify MECO horizon from our bulk $\delta^{13}C$ record.

4.2 Bulk chemical compositions

The bulk chemical composition data of Site 762C, including TC, TOC, and $CaCO_3$ content, are shown in Supporting Table S4. The results show that Ca is the most abundant element in the samples of Site 762C (Ca = 23.7–38.9 wt.%), and $CaCO_3$ accounts for 60.2–93.3 wt.% of bulk samples. Among the other major elements, Fe and Al are contained in percent order (Al = 0.297–2.23 wt.%; Fe = 0.180–2.13 wt.%). In the trace element composition (elements in the order of ppm), Sr and Ba show considerably high concentrations (Sr = 580–1308 ppm; Ba = 366–1683 ppm) compared to other trace elements.

In the depth profile of each element, the concentration of $CaCO_3$, the most abundant component in the studied samples, dropped at the horizons of negative $\delta^{13}C$ and $\delta^{18}O$ excursions (395, 390, 379, and 373 mbsf; Figure 3b, c). In addition, the $CaCO_3$ abundance also dropped at 422, 373, and 288 mbsf (Supporting Figure S2a). Conversely, depth profiles of detrital-origin elements (e.g., Ti, Al) are correspondingly symmetric to that of $CaCO_3$ (Supporting Figure S3). The depth profiles of P, Y, and total rare earth elements (REEs; here indicating from La to Lu) were similar and showed sharp peaks at 404, 373, and 331 mbsf. Some metal elements (e.g., Cu, Pb) showed several spike-like peaks in the depth profiles (Supporting Figure S3). Except for each peak, these elements generally showed relatively less variable profiles in the long-term trend.

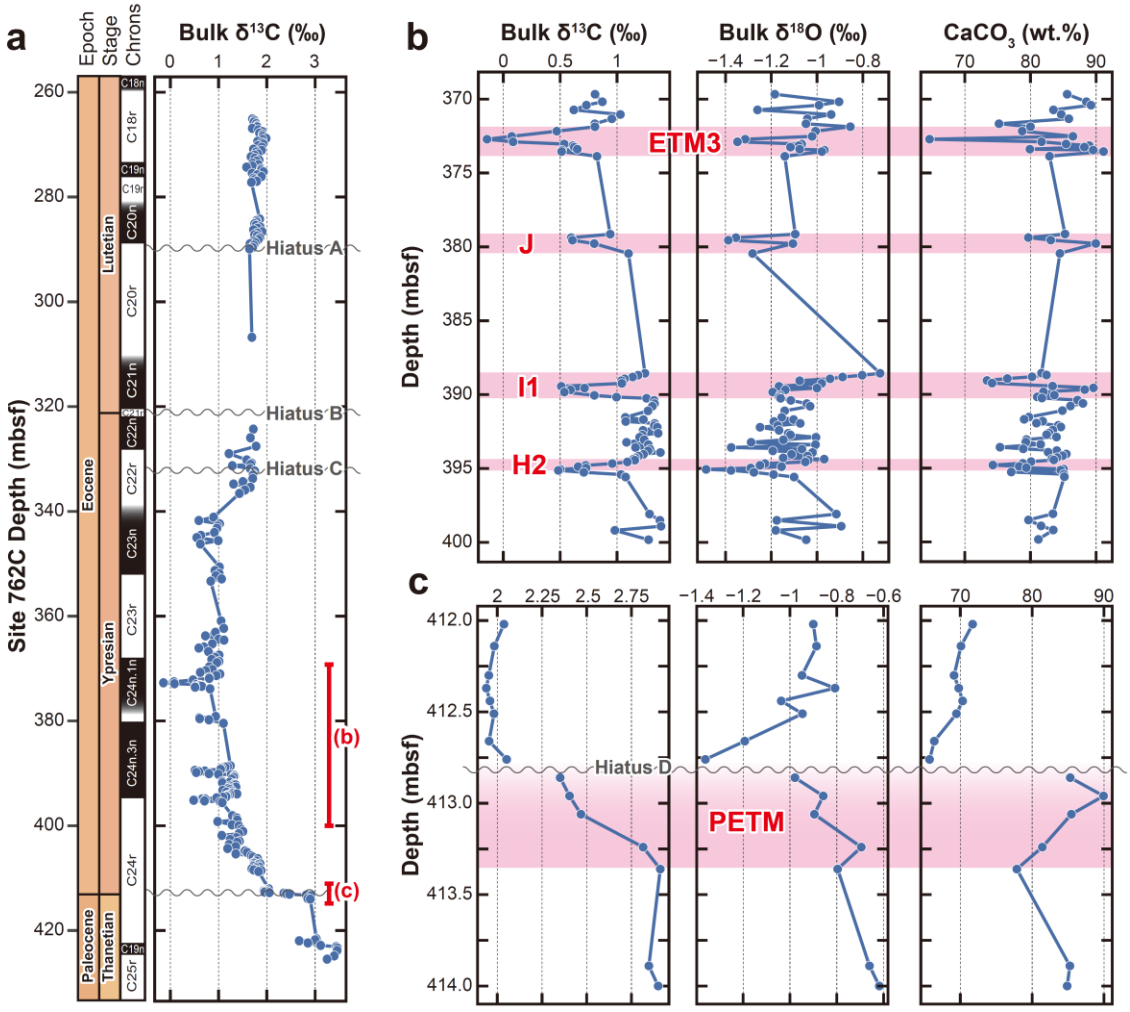

Figure 3. Depth profiles of bulk $\delta^{13}C$, $\delta^{18}O$, and $CaCO_3$ of Site 762C. (a) All data. (b) Data from early Eocene (Core 25X–23X). (c) Data around Paleocene–Eocene boundary (Core 28X). Intervals with red lines indicate ranges of panels (b) and (c). Analytical uncertainties of $\delta^{13}C$ and $\delta^{18}O$ are less than 0.02‰ and 0.04‰, respectively. In panel (a), magnetostratigraphic columns and identified hiatuses are also shown (Shamrock et al., 2012).

4.3 Independent Component Analysis

In this study, we implemented ICA on a dataset consisting of 40 elements and 248 samples from Site 762C. The relative IC loadings are presented in Figure 4. It should be noted that the numbering of ICs is arbitrary and commutative and does not indicate their mutual importance. The scatterplots depicting the relationships between ICs indicate clear orthogonality among the six components, demonstrating their statistical independence from one another (Supporting Figure S4). The validity of extracting six ICs is discussed on Supporting Text S1 in detail. Our subsequent discussion is based on the results corresponding to the six ICs (Figure 4).

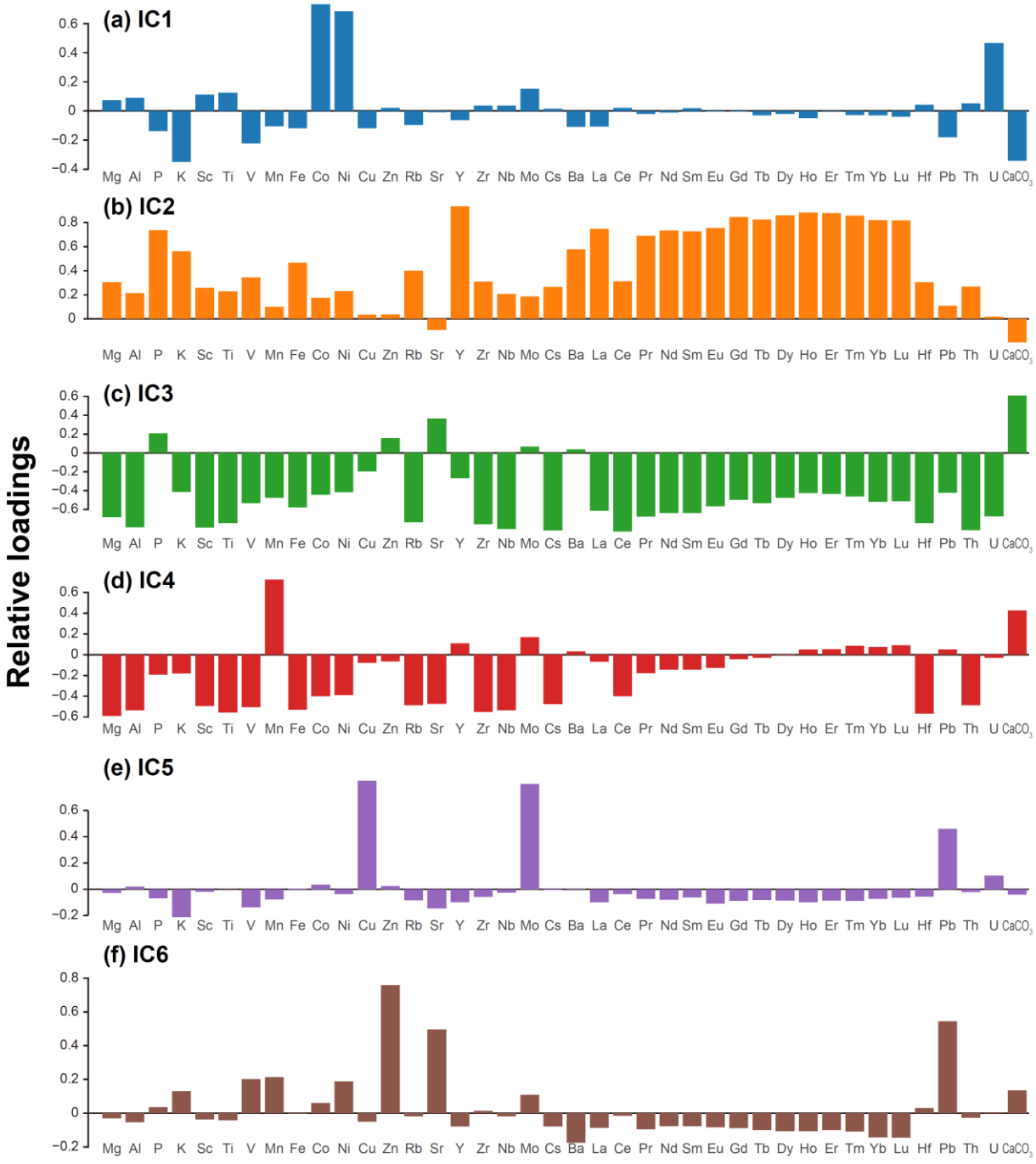

Figure 4. IC loadings of major and trace elements obtained from the Site 762C dataset when the number of ICs = 6.

5 Discussion

5.1 Revision of the Age Model

Although previous studies have suggested that Site 762C sediments contain multiple hyperthermal horizons (Shamrock et al., 2012; Thomas, 1992; Xu et al., 2021), the precise identification of hyperthermal events has not been achieved owing to the limited temporal resolution of previous bulk $\delta^{13}C$ and $\delta^{18}O$ records. Thus, the age model of Site 762C must be further considered.

In this study, we identified the hyperthermal horizons of Site 762C using the newly obtained bulk carbonate $\delta^{13}C$ and $\delta^{18}O$ records in combination with the age constraint by magnetostratigraphy and biostratigraphy of Site 762C (Shamrock & Watkins, 2012; Shamrock et al., 2012; Figure 2a) and the well-established compilation of benthic foraminifera $\delta^{13}C$ records "CENOGRID" (Westerhold et al., 2018, 2020; Figure 2b). Consequently, we identified at least five hyperthermals (PETM, H2, I1, J, and ETM3) in the studied section of Site 762C. We described the base of identifying each hyperthermal horizon on Supporting Text S2. As previous age models of Site 762C did not include the horizons of I1 and J events (Shamrock et al., 2012; Thomas, 1992; Xu et al., 2021) and are based on not up-to-date magnetostratigraphic age, we updated the age model of Site 762C using newly identified hyperthermal horizons and revised magneto- and biostratigraphic ages by "Geologic Time Scale 2020 (GTS2020; Speijer et al., 2020)" and Westerhold et al. (2020). The updated age-tie points are presented in Supporting Table S5.

Previous studies inferred that the Middle Miocene Climate Optimum (MECO) horizon exists in Cores 12X and 13X (284.0–265.0 mbsf), the uppermost part of the studied section of Site 762C, based on the nannofossil assemblages (Shamrock et al., 2012; Shamrock & Watkins, 2012). The MECO was a one-million-year warming event characterized by a positive anomaly in $\delta^{13}C$ and a negative anomaly in $\delta^{18}O$ (e.g., Henehan et al., 2020; Sluijs et al., 2013). However, such excursions were not clearly observed in our bulk $\delta^{13}C$ and $\delta^{18}O$ records; thus, we cannot identify the chemostratigraphic evidence of the MECO horizon (Figure 2). Therefore, we determined that the age-tie points are based on magneto- and biostratigraphic ages without $\delta^{13}C$ chemostratigraphy during the middle Eocene intervals (Speijer et al., 2020; Westerhold et al., 2020)

Based on the age determination in this study, the depositional ages of studied samples from Site 762C were estimated to be from 57.61 Ma (Late Paleocene: Thanetian) to 39.06 Ma (Middle Eocene: Bartonian; Figure 5). The sedimentation rate at Site 762C was calculated to be 0.6–44.6 m/Ma (Supporting Figure S8: Table S5). The extremely high sedimentation rate at Core 29X (77.9 m/Ma; 439.26–424.45 mbsf) could be due to the presence of voids in the core (424.50–424.15 mbsf; Core 29X-2 115–150 cm) and core fragmentation (Haq et al., 1990).

5.2 Long-term Variation of Bulk Carbonate $\delta^{13}C$ and $\delta^{18}O$ Records

The bulk carbonate $\delta^{13}C$ of sediments reflects those of dissolved inorganic carbon in seawater incorporated into the $CaCO_3$ (e.g., Luciani et al., 2016). As the studied samples from Site 762C are nannofossil chalk consisting of the coccoliths of calcareous phytoplankton (Haq et al., 1990), the bulk carbonate $\delta^{13}C$ record of Site 762C can be interpreted as the $\delta^{13}C$ of near-surface seawater.

A comparison of the long-term trends of the bulk carbonate $\delta^{13}C$ records of Site 762C with the global compilation of $\delta^{13}C$ records of benthic foraminifera (i.e., $\delta^{13}C$ of deep seawater; Westerhold et al., 2020) revealed that the bulk carbonate $\delta^{13}C$ records of Site 762C were ~1‰ higher than those of benthic $\delta^{13}C$ records throughout the studied period (Late Paleocene–Middle Eocene; Figure 5a). This feature suggests that the ocean surface layer exhibits higher $\delta^{13}C$ than the deeper layers, which may indicate that deep seawater contains a larger amount of isotopically light carbon derived from the decomposition of organic matter compared to near-surface seawater (e.g., Ravizza & Zachos, 2014).

The long-term decrease of bulk $\delta^{13}C$ records of Site 762C from ~57.5 Ma (~3.3‰) to ~53.0 Ma (~0.0‰), as seen in CENOGRID benthic $\delta^{13}C$ records, could be interpreted as the long-term increase in the net release of isotopically light carbon to the deep ocean (e.g., Kirtland Turner et al., 2014; Komar et al., 2013). Among several explanations for the $\delta^{13}C$ decrease proposed by previous studies, one of the leading hypotheses is the continuous release of carbon due to the decomposition of organic matter (e.g., biogenic CH_4, permafrost, and peat) triggered by the orbital pacing (e.g., Barnet et al., 2019; Kirtland Turner et al., 2014; Komer et al., 2013). Our data indicate that the $\delta^{13}C$ decrease toward ~53 Ma is also a common phenomenon on the surface of the eastern Indian Ocean.

The ~1‰ increase of bulk carbonate $\delta^{13}C$ of Site 762C during the magnetic polarity Chron C23n (52–51 Ma) is also commonly observed in the global benthic $\delta^{13}C$ data (Figure 5a; Westerhold et al., 2020), although there is ~400 kyr difference between them. The timing lag in the rise of $\delta^{13}C$ of Site 762C during C23n could be attributed to the age uncertainty and poor core recovery in Core 19X, corresponding to C19n (64.8%; Haq et al., 1990). To date, several debatable hypotheses, including increased carbon burial flux, changes in oceanographic circulation patterns, and active volcanism, attempt to explain the rise of $\delta^{13}C$ during C19n (Anagnostou et al., 2020; Westerhold et al., 2018). A global-scale upheaval of the terrestrial environment (e.g., temperature, precipitation rate; Hyland et al., 2017; Hyland & Sheldon, 2013) and tectonic events, including the change of the orientation of plate motion and generation of new subduction zone (e.g., Ishizuka et al., 2011; O'Connor et al., 2013; Whittaker et al., 2007) have been reported during Chron C23. These tectonic or environmental changes could contribute to changes in global carbon cycle involving the rise of seawater $\delta^{13}C$.

During 50–41 Ma, the $\delta^{13}C$ record did not show long-term changes, indicating the absence of long-term changes in the carbon cycle. While previous studies reported the increase in $\delta^{13}C$ during 40.5–39.5 Ma known as MECO (Henehan et al., 2020; Sluijs et al., 2013; Westerhold et al., 2020), our Site 762C cores did not show such increase in $\delta^{13}C$ record. This may be due to the age uncertainty due to the coring gap or hiatuses.

386 The bulk carbonate $\delta^{18}O$ of Site 762C seems to indicate a general SST trend because the
387 core consists mainly of the calcareous nannofossil, although the $\delta^{18}O$ value might be affected by
388 diagenetic processes or the contribution of other components. The long-term variation of bulk
389 $\delta^{18}O$ at Site 762C shows a gradual decrease from the late Paleocene (~ –0.7‰) to ~52.5 Ma (~ –
390 1.3‰), suggesting the long-term rise of SST toward the EECO, as previously reported (Figure
391 5b; Shamrock et al., 2012). After the peak of EECO, the bulk $\delta^{18}O$ of Site 762C increases until
392 ~47 Ma (~0.0‰), which can be interpreted as the cooling of SST, corresponding to the Mid-
393 Eocene Cooling. From 47 Ma to 38 Ma, the bulk $\delta^{18}O$ of Site 762C fluctuates between 0‰ and
394 0.5‰, suggesting no significant variation of SST in this period, indicating that the studied
395 samples from Site 762C did not record the warm period of MECO (~40.5 Ma) indicated in
396 globally compiled benthic record (Henehan et al., 2020; Sluijs et al., 2013; Westerhold et al.,
397 2020).

398 Contrary to the $\delta^{13}C$, the trend of bulk $\delta^{18}O$ of Site 762C is different from those of
399 benthic $\delta^{18}O$ records (Westerhold et al., 2020). During the EECO period, the gap between bulk
400 $\delta^{18}O$ of Site 762C (i.e., SST at Site 762C) and benthic $\delta^{18}O$ (i.e., a global signature of deep
401 seawater temperature) narrows toward ~50 Ma (Figure 5b). This feature is also observed in the
402 Southern Ocean (ODP Sites 690 and 738; Auderset et al., 2022), Atlantic Ocean (DSDP 550;
403 Charisi & Schmitz, 1996), and the Pacific Ocean (ODP Site 1209; Dutton et al., 2005).
404 Assuming that benthic $\delta^{18}O$ is globally homogeneous (Westerhold et al., 2020), the narrowing
405 gap between bulk $\delta^{18}O$ of Site 762C and globally compiled benthic $\delta^{18}O$ implies that the
406 vertical gradient of temperature and density in the water column decreased during the EECO.

407

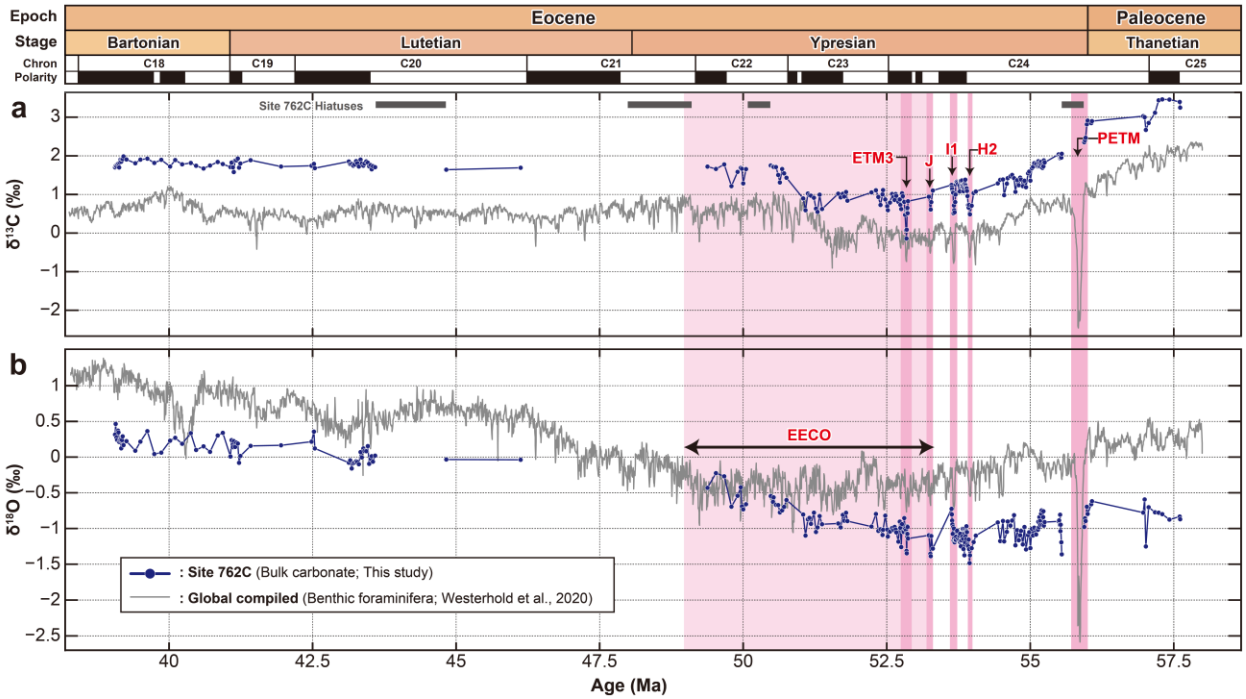

Figure 5. Age profiles of bulk $\delta^{13}C$ and $\delta^{18}O$ of Site 762C. Grey lines indicate global compiled $\delta^{13}C$ and $\delta^{18}O$ of benthic foraminifera (Westerhold et al., 2020). Polarity chron is also shown on the top. Vertical red bars indicate hyperthermals and EECO.

5.3 Variation of Bulk $\delta^{13}C$ and $\delta^{18}O$ Records during Hyperthermals

Compared with other marine and terrestrial records of the bulk carbonate $\delta^{13}C$ record of hyperthermal events (excluding the PETM), the bulk carbonate $\delta^{13}C$ at Site 762C exhibited generally consistent behavior and magnitudes with records from the Atlantic, Pacific, and Indian Oceans. The magnitude of the CIE during the H2 event at Site 762C (~0.6‰; Figure 3b) is comparable to the bulk carbonate data from northeastern Atlantic (~0.4‰: DSDP Site 550; Cramer et al., 2003), northwestern Atlantic (~0.5‰: Blake Nose - ODP Sites 1051; Cramer et al., 2003), southern Atlantic (~0.6‰: Walvis Ridge - ODP Sites 1263, 1265, and 1267; Stap et al., 2009; Westerhold et al., 2017), and the southern Indian Ocean (~0.5‰: Kerguelen Plateau - ODP Site 738C; Yasukawa et al., 2017). However, records from the central Pacific (~0.3‰: DSDP 577; Cramer et al., 2003; Luciani et al., 2016) and the southern Pacific (~0.2‰: Mead Stream, Dee Stream; Nicolo et al., 2007) exhibit smaller CIEs compared to that of Site 762C.

Regarding the I1 Events, the CIE at Site 762C (~0.7‰) is comparable to other regions' data. Similar CIE magnitudes have been reported from the Atlantic (~0.7‰: DSDP 550, ODP Sites 1051, 1262, 1263; Cramer et al., 2003; Westerhold et al., 2017), Pacific (0.5–0.6‰: DSDP 577, Mead Stream, Dee Stream; Cramer et al., 2003; Nicolo et al., 2007), and southern Indian Oceans (~0.6‰: ODP Sites 752 and 738C; Yasukawa et al., 2017). In Site 762C, the CIE magnitude during the J event (~0.5‰) is similar to that of the Atlantic record (~0.5‰: DSDP 550, ODP Sites 1262, 1263; Cramer et al., 2003; Westerhold et al., 2017) and the Pacific record (~0.4‰: DSDP 577; Luciani et al., 2016). The largest CIE (~0.9‰) was observed during the

ETM3 horizon in Core 25X of Site 762C sediments. This magnitude is similar to that of the Atlantic (0.6–1.0‰: DSDP 550, ODP Sites 1262, 1263; Cramer et al., 2003; Westerhold et al., 2017), central Pacific (0.7–1.0‰: DSDP 577, ODP Site 1215; Leon-Rodriguez & Dickens, 2010; Luciani et al., 2016), and southern Indian Ocean records (~0.9‰: Site 752; Yasukawa et al., 2017). As the magnitude of CIEs at Site 762C is comparable to that of other regions' data, we can consider that the geochemical records of the modest Eocene hyperthermals at Site 762C are well preserved without hiatus or truncation.

5.4 Interpretation of ICs Extracted from Bulk Chemical Composition

5.4.1 IC3: Dilution between Biogenic $CaCO_3$ and Detrital Components

The IC3 shows positive $CaCO_3$ and Sr loadings and negative loadings of most other elements (Figure 4c). The age profile of the IC3 score is similar to that of $CaCO_3$ abundances (Supporting Figure S9). These features indicate that the positive side of IC3 represents the biogenic $CaCO_3$ component that constitutes the main component of the Site 762C sediment. As Sr is an alkaline earth metal that can be easily incorporated into biogenic carbonates, Sr is known to coexist with Ca in carbonate sediments (e.g., Plank & Langmuir, 1998; Rudnick & Gao, 2014). Conversely, elements showing distinct negative loadings (e.g., Mg, Al, Ti, Rb, Zr, Nb, Cs, Hf, Th, and light rare earth elements [LREEs]), which are commonly contained in aluminosilicates, indicate the contribution of detrital components. Therefore, IC3 appears to indicate a mixing relationship between biogenic $CaCO_3$ and detrital component as one of the major structures in our dataset.

5.4.2 IC2: Biogenic Calcium Phosphate

The IC2 shows positive loadings of P and REY except for Ce (Figure 4b). This feature indicates that the IC2 extracts a biogenic calcium phosphate (BCP) component in the sediment. Biogenic calcium phosphate, a common component in marine sediments, is contained in bones, teeth, and scales of marine vertebrates. As BCP effectively adsorbs REE and Y from ambient seawater, REE and Y are highly concentrated in BCP in marine sediments (Kashiwabara et al., 2014; Takaya et al., 2018; Toyoda & Tokonami, 1990). Indeed, the Al-normalized P and Y abundances of Site 762C show identical age profiles and have a strong positive correlation (r = 0.91; Supporting Figure S9), suggesting that the excess P and Y (or REE) relative to detrital materials can be explained by BCP contribution. Therefore, the significant positive loadings of P and REE in IC2 may reflect the influence of BCP on the bulk sediment composition. In addition, the small Ce loading and large loadings of Y and heavy rare earth elements (HREEs) on the positive side of IC2 loadings appear to be a similar pattern to the shale-normalized REY composition of seawater (Alibo & Nozaki, 1999). Therefore, the BCP components in Site 762C sediment are considered to contain REE and Y of seawater origin. Notably, in the age profiles of IC scores (Figure 6; Supporting Figure S9), IC2 does not show a mirror profile of the $CaCO_3$ and IC3. Therefore, the variation of IC2 scores does not simply reflect a simple dilution of BCP abundance by biogenic $CaCO_3$. Instead, it is controlled by various environmental factors that influence the accumulation rate of BCP at Site 762C.

5.4.3 IC4: Diagenetic Signature on Carbonate

The IC4 demonstrates positive loadings of Mn and $CaCO_3$ (Figure 4d). The abundance of Mn has been utilized as an indicator of diagenetic processes because its solubility is affected by the redox conditions in the sediment. In the oxic environment, Mn occurs as MnO_2 in sediments; under reducing conditions caused by the consumption of dissolved oxygen via organic matter decomposition, Mn dissolves in pore water as Mn^{2+} (e.g., Burdige & Gieskies, 1983; Calvert & Pederson, 1993). In carbonate sediments, dissolved Mn^{2+} can be incorporated into or precipitate as (Mn, Ca)CO_3 on the surface of biogenic $CaCO_3$ shells (e.g., Barras et al., 2018; Boyle, 1983; Thomson et al., 1986, 1993; Pälike et al., 2014). Based on these behaviors of Mn in marine sediments and the positive correlation between Mn and $CaCO_3$ in the IC4, the positive loadings of IC4 can be interpreted as the incorporation of Mn by $CaCO_3$ through the diagenetic process at Site 762C. Overall, we interpreted that IC4 represents the diagenetic signature involving redox changes in the Site 762C sediments.

5.4.5 IC1, IC5, IC6: Redox-related Behaviors of Metal Elements

IC1, IC5, and IC6 are characterized by specific metals, including Co, Ni, U, Cu, Mo, Pb, Zn, and Sr (Figure 4a, e, f). The age profiles of IC1, IC5, and IC6 scores exhibit spike-like excursions at particular horizons (e.g., hyperthermals), indicating that the concentration/depletion of these metal elements occurred at those horizons (Figure 6b, c; Supporting Figure S10). These features suggest that IC1, IC5, and IC6 may indicate redox-related signatures in Site 762C sediments because these metals exhibit specific abundances in sediments corresponding to the ambient redox state. The elements characterizing IC1, IC5, and IC6 (except Sr) are categorized as the “redox-sensitive elements” that exhibit characteristic reconcentration patterns in sediments due to the changes of valences corresponding to the redox state in the sediment pore water. Therefore, redox-sensitive elements are concentrated or depleted at the boundary between oxic and suboxic conditions in the sediments and utilized as the indicator of the redox state in the sediments (e.g., Calvert & Pederson, 1993; Thomson et al., 1993).

Various behaviors of such redox-sensitive metals have been proposed to explain their concentration/depletion in marine sediments, including remobilization and precipitation of metals due to the change of valence corresponding to the redox state of sediment pore water (e.g., Calvert & Pederson, 1993) and co-precipitation with authigenic pyrite (Algeo & Maynard, 2004; Huerta-Diez & Morse, 1992). The separation between IC1, IC5, and IC6 may reflect differences in the concentration/depletion processes described above.

IC1 is distinguished by positive Co, Ni, and U loadings, and its score indicates positive excursions at horizons near Hiatus D, I1, and J (Figure 6b, c). The age profile of the IC1 score closely matches that of the Co/Al and Ni/Al profiles, except for the I1 horizon (Supporting Figure S10b, c), strongly suggesting that IC1 reflects the variation of Co and Ni in the sediments. The presence of authigenic pyrite and the positive loading of U (Figure 4a), indicating a reduced porewater environment, suggests that the elevation of Co and Ni abundances, as indicated by the IC1 peaks, may be associated with the precipitation of sulfides (e.g., pyrite) (Huerta-Diez & Morse, 1992; Swanner et al., 2019). As the uptake of Co and Ni into pyrite occurs more slowly compared to other redox-sensitive elements (Algeo & Maynard, 2004), the peaks of IC1, corresponding to those of Co and Ni, may be attributed to the kinetic differences from other redox-sensitive elements (e.g., Cu, Mo, and Pb) (Figure 6c).

516 Positive loadings of Cu, Mo, and Pb characterize IC5 (Figure 4e). Its score exhibits
517 positive excursions at the horizons near Hiatus D, ~55 Ma, H2, and I1 (Figure 6b, c). Conversely,
518 IC6 is characterized by the positive loadings of Zn, Sr, and Pb (Figure 4f), and its scores show
519 positive excursions at horizons near Hiatus D, I1, and ETM3. In addition, the IC6 score also
520 shows two excursions during 41–39 Ma (Figure 6a). Based on the element assemblages of IC5
521 and IC6 and the behavior of their scores, the IC5 and IC6 may reflect the remobilization and
522 reconcentration of redox-sensitive elements due to the change of redox (or pH) conditions in the
523 sediments.

524 The enrichment of Co, Ni, Cu, Mo, Zn, and Pb in marine sediments is also caused by the
525 co-precipitation of authigenic pyrite under reductive conditions, although the uptake speed varies
526 by element (e.g., Algeo & Maynard, 2004; Huerta-Diez & Morse, 1992). Indeed, at the horizons
527 showing positive peaks of IC1, IC5, and IC6, we observed authigenic pyrite grains as suggested
528 by the onboard visual core description of Site 762C sediments (Haq et al., 1990). Therefore, it is
529 also possible that the excursions of these three ICs reflect the occurrence of pyrite precipitation.
530 Although pyrite precipitation or redox-related valence changes of metal elements are difficult to
531 distinguish from the bulk chemical composition, the variation and excursions of IC1, IC5, and
532 IC6 scores can be interpreted as the redox (and/or pH) changes in the pore water.

533 Based on the above discussion, we interpreted that IC1, IC5, and IC6 reflect the post-
534 depositional processes related to the changes in the sediments' redox (or pH) conditions.
535 Therefore, in the following sections, we consider these three ICs as an indicator of the
536 geochemical condition of pore water.

537

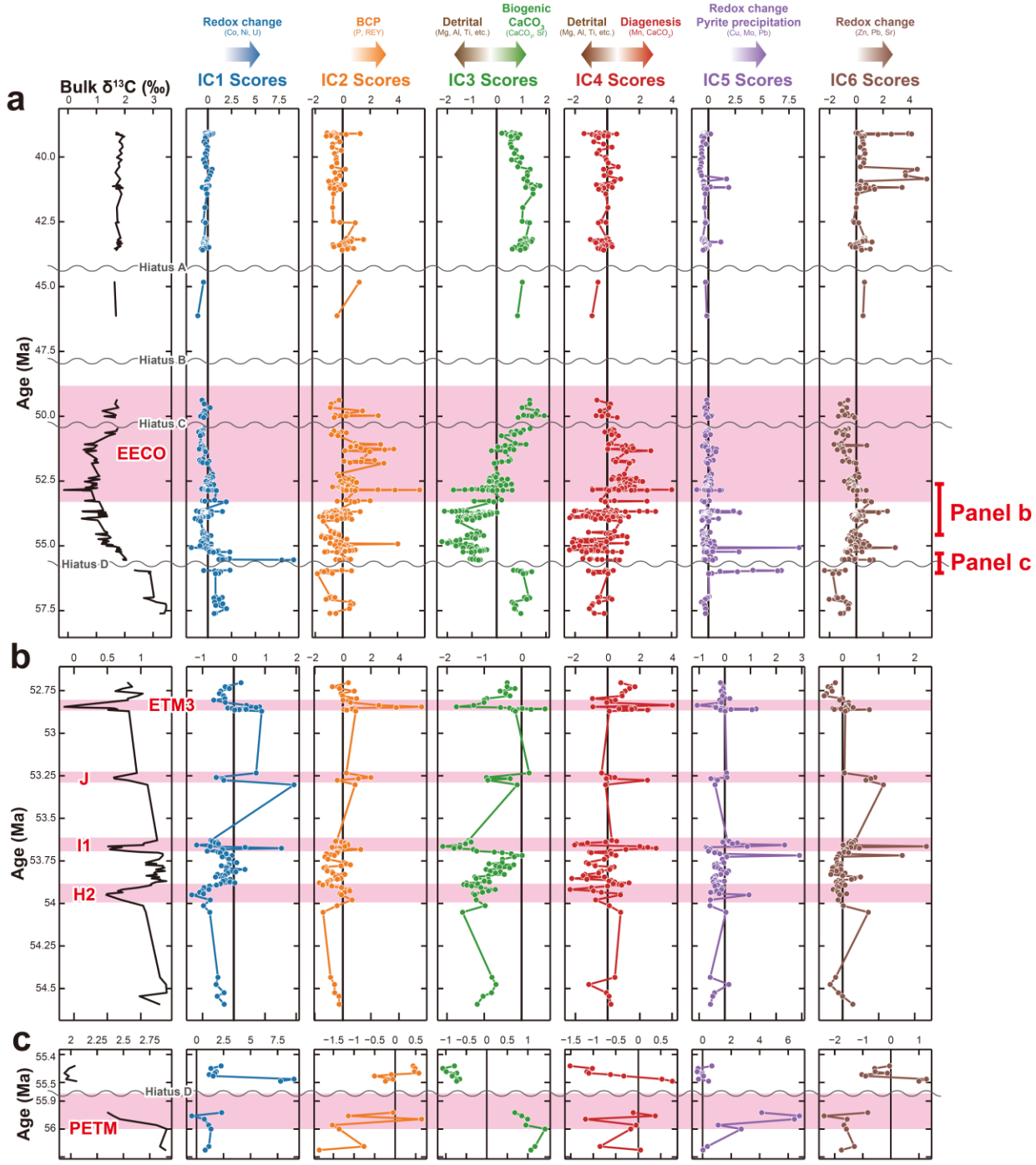

Figure 6. Age profiles of extracted ICs from the bulk chemical composition and bulk $\delta^{13}C$ of ODP Site 762C. (a) Whole studied sections. (b) Sections covering multiple hyperthermals (H2, I1, J, and ETM3). (c) A section covering the PETM. Grey lines in each panel indicate bulk carbonate $\delta^{13}C$ records. Horizontal pink bars in panel (a) indicate EECO, and in panels (b) and (c) indicate hyperthermals. Grey waved lines are hiatuses indicated by Shamrock et al. (2012).

5.5 Geochemical Implication of Each IC for Long-Term Trends

The IC2 and IC3 show long-term variations throughout the studied section, while the remaining ICs only show transient spike-like excursions. In this section, we discuss the long-term trends of IC2 and IC3.

5.5.1 Change of $CaCO_3$ Contribution Associated with Long-Term Climate Changes

IC3, which reflects the mixing relationship between biogenic $CaCO_3$ and detrital component, exhibited significant variations on the long timescale. Considering that the paleodepth of Site 762C did not show large variations throughout the Cenozoic (1000–1200 m; Haq et al., 1992; Jones & Wonders, 1992), the variation of IC3 scores was not largely affected by changes in paleodepth. In addition, because the location of Site 762C is a passive margin without a large change in the paleogeography (especially the distance to the continent) throughout the studied period (e.g., Scotese, 2001; Figure 1a), the secular changes in tectonic settings can be negligible for changes in the supply of detrital components to Site 762C. Therefore, we considered that the variation in IC3 scores was not mainly caused by tectonic factors but by climatic or paleoceanographic changes.

Over the long-term, the IC3 score decreased between 56 and 55 Ma, followed by a gradual increase during 53–50 Ma (Figure 6a). Then, the IC3 scores kept a high value (~ 1) during 50–42 Ma and showed a slight decline towards ~ 39 Ma. In addition, scatter diagrams show that IC3 scores show positive correlations with bulk $\delta^{18}O$ (r = 0.70; Supporting Figure S11d). This indicates that the relative contribution between biogenic $CaCO_3$ and detrital components at Site 762C fluctuated in accordance with long-term climate changes in the southeastern Indian Ocean, such as the EECO and subsequent cooling.

One interpretation of the long-term variation in IC3 scores is the fluctuation in the depositional rate of $CaCO_3$ associated with the early Paleogene climate. Paleo-CCD estimation from the Pacific and Indian Oceans suggest that shallowing of CCD occurred under high (~1,100–3,000 ppmv) atmospheric pCO_2 and low pH seawater during the EECO (Anagnostou et al., 2016; Pälike et al., 2012; Slotnick et al., 2015). While it is unlikely that the CCD became shallower than the paleodepth of Site 762C during the study period, low IC3 scores in the earliest Eocene could be attributed to a reduced flux of carbonate precipitation to the seafloor because of changes in the paleoceanographic environment, such as vertical mixing, pH levels, and dissolved oxygen concentrations, in the water column, during this period (Luciani et al., 2017). Curiously, the increase in bulk carbonate $\delta^{18}O$ and IC3 score precedes (by ~2.5 Myr) that of global-compiled benthic $\delta^{18}O$ record noted as the end of EECO (see Section 5.2., Figure 5b; Westerhold et al., 2018, 2020). Given that previous studies have reported a reduction in the difference between benthic and planktonic $\delta^{18}O$ during the EECO and have interpreted it as a collapse of oceanic stratification (Auderset et al., 2022; Charisi & Schmitz, 1996; Dutton et al., 2005), increases in bulk carbonate $\delta^{18}O$ and IC3 score at Site 762C may suggest that the collapse of the vertical structure of the water column (e.g., temperature, pH, and salinity) occurred at the Exmouth Plateau and affected the precipitation flux of biogenic $CaCO_3$. Indeed, micropaleontological studies have shown that the turnover of the nannofossil and planktonic

foraminifera assemblages occurred at the surface ocean associated with major climatic changes, including the PETM and EECO (Luciani et al., 2016, 2017; Shamrock & Watkins, 2012), suggesting that climate shift impacted the sea-surface ecosystems, especially carbonate shell-forming organisms.

The increase in IC3 score may also reflect a decrease in the influx of terrigenous material. Under the warm climate and enhanced hydrological cycle during the early Eocene, it has been suggested that the supply of terrigenous materials into the ocean was accelerated (e.g., Dallanave et al., 2015; Hyland and Sheldon, 2013). Therefore, the decrease in IC3 score during ~56–55 Ma can be interpreted as an increase in terrigenous input relative to $CaCO_3$. Indeed, the upper continental crust (UCC)-normalized REE pattern, which is an indicator of detrital contribution in marine sediments (e.g., Murray et al., 1991; Plank & Langmuir, 1998), also indicates an increase in detrital components in Site 762C sediments during the warm climate of Earliest Eocene. We used Ce/Ce* as an index of Ce negative anomalies (Ce/Ce*) defined as:

$$\frac{\mathrm{Ce}}{\mathrm{Ce}^*} = \frac{\mathrm{Ce_N}}{\sqrt{\mathrm{La_N Pr_N}}} \quad (3)$$

where the subscript "N" indicates the UCC-normalized value (Rudnick & Gao, 2014), and Y_N/Ho_N as an index of Y positive anomalies. Both indices showed clear correlations with IC3 scores (Ce/Ce*: $r = -0.78$, Y_N/Ho_N: $r = 0.81$; Supporting Figure S11e, f). The Ce/Ce* and Y_N/Ho_N also showed correlations with $\delta^{18}O$ ($r = -0.46$, 0.73, respectively). The negative Ce and positive Y anomalies in UCC-normalized REY patterns indicate the signature of seawater (e.g., Alibo & Nozaki, 1999; Bolhar et al., 2004; De Baar et al., 1985), while the smaller anomalies or relatively flat REE patterns indicate a high contribution of the terrigenous material. Therefore, the correlations between $\delta^{18}O$ and Ce/Ce*, as well as Y_N/Ho_N in sediments from Site 762C, indicate that there was an increase in terrigenous input during the warm period of the earliest Eocene (approximately 56–55 Ma) followed by a decrease as the cooling proceeded toward the middle Eocene.

Considering that climatic and hydrological patterns might have significantly changed in the EECO, the low IC3 score during the earliest Eocene, followed by an increase in the score, can be interpreted as a decrease in terrigenous (i.e., riverine and aeolian) input to the depositional area associated with the cooling trend toward the middle Eocene. As the major source of aeolian dust at the Exmouth Plateau during the Quaternary is considered to be inland arid areas of the Australian Continent (e.g., Gascoyne plain) (Hasse & McTainsh, 2003), the aeolian dust supply to the early Eocene sediments at Site 762C could also be derived from Australia. However, in contrast to the arid environment in modern Australia, the early–middle Eocene terrestrial environment of the Australian continent was considered to be warmer with a more active hydrological cycle than that of the present (Reichgelt et al., 2022). If we consider that the aridification of the Australian continent progressed in relation to the early–middle Eocene cooling, it would be expected that the dust influx to the Exmouth Plateau would increase, leading to an increased contribution of detrital material in the sediments. However, the time-series profile of the IC3 score suggests the opposite behavior (Figure 6a); the dust supply into the Exmouth Plateau could be diminished by cooling toward the middle Eocene. A possible explanation is that the influence of the aeolian dust flux on the variation in IC3 was minor. In contrast, riverine detrital material could have affected the IC3 scores. It has been reported that

the contribution of terrigenous fluvial input into the deep-sea sediments around the continent has increased during the earliest Eocene and EECO (Burton et al., 2023). Thus, enhanced denudation, drainage, and chemical weathering in the warm and humid terrestrial environment in the early Eocene may have caused an increase in riverine input of terrigenous materials to the coastal area and, thus, low values in the IC3 score at Site 762C.

Overall, the long-term variation in IC3 scores indicates changes in terrigenous (especially fluvial) input or marine ecosystems (especially the abundance of carbonate-bearing organisms) associated with climatic changes, namely the EECO and subsequent cooling.

5.5.2 Long-Term Biogenic Calcium Phosphate Abundances

The IC2 score, which reflects the contribution of BCP, shows a tendency to increase during the EECO period, particularly in 51–50 Ma (Figure 6a). Although scatter diagrams do not exhibit clear negative correlations between IC2 and $\delta^{13}C$ and $\delta^{18}O$ (r = –0.39, –0.21, respectively; Supporting Figure S11a, b), samples from the EECO (including ETM3 horizon) show high scores. This feature suggests that the high-level consumers, typically vertebrates such as fish, in the marine ecosystems prospered under the warm environment of EECO at Site 762C. This finding is consistent with previous studies demonstrating an increase in fish population during warm environments in the early Eocene based on ichthyolith accumulation rates in pelagic sediments (Britten & Sibert, 2020; Sibert et al., 2016). Our study indicates that such proliferation of marine vertebrates coherently occurred in relatively coastal regions.

5.6 Geochemical Implication of Each IC on Hyperthermals

5.6.1 Change of $CaCO_3$ Contribution Associated with Hyperthermals

On a shorter (~10^5 yr) timescale, IC3 scores exhibited several spike-like decreases, typically at the I1, J, and ETM3 horizons (Figure 6b). These features indicate a decrease in the contribution of biogenic $CaCO_3$ at multiple hyperthermal horizons at Site 762C. As it is well known that ocean acidification and shallowing of CCD occurred during hyperthermal events (e.g., Slotnick et al., 2015; Zachos et al., 2005, 2010), the decrease in IC3 scores associated with carbon isotope excursions (CIEs) at multiple hyperthermal horizons may reflect the repetitive shallowing of the CCD at Site 762C. Additionally, an increase in detrital input may also contribute to a decrease in the IC3 score during hyperthermals. As it has been argued that the weathering of terrestrial material increased during the hyperthermals (e.g., Ravizza et al., 2001; Tanaka et al., 2022), we cannot exclude the possibility of an increase in detrital input into the depositional area of the Site 762C.

In contrast to the record at Site 762C, a previous study that applied ICA to early Eocene carbonate sediments from the southern Indian Ocean (ODP Sites 752 and 738C) did not show clear negative excursions of IC scores reflecting biogenic $CaCO_3$ content at H2, I1, and ETM3, despite the paleo-depth of both sites being close to that of Site 762C (~1000–1300 m; Yasukawa et al., 2017). Therefore, the magnitude of the reduction in carbonate rain flux due to CCD shallowing or the increase in detrital materials during hyperthermals could have been regionally variable.

The H2 horizon at Site 762C did not exhibit a clear negative excursion of IC3 scores and $CaCO_3$ abundances (Figure 6b; Supporting Figure S9b). The relatively minor variation at the H2 horizon compared to that at the I1, J, and ETM3 horizons indicates that the magnitude of CCD shallowing and the reduction of carbonate rain flux during the H2 event were smaller than those during other events. This feature is consistent with the Atlantic record (Walvis Ridge; Stap et al., 2009, 2010) and suggests that the magnitude of CCD shallowing could have been variable between each hyperthermal.

5.6.2 Biogenic Calcium Phosphate Contribution Associated with Hyperthermals

In the sediments of Site 762C, the IC2 score repetitively showed spike-like increases at the PETM (onset), H2, I1, J, and ETM3 horizons (Figure 6b, c). As IC2 primarily reflects the contribution of BCP, the systematic increase in IC2 scores at hyperthermal horizons indicates an increase in the contribution of BCP associated with the warming events. Therefore, the proliferation of fish at Site 762C could be associated with hyperthermals.

There have been arguments about whether or not biological productivity was enhanced during hyperthermals (e.g., Bains et al., 2000; Bralower, 2002; Gibbs et al., 2006; Ma et al., 2014; Winguth et al., 2012; Yasukawa et al., 2017; Zhou et al., 2014). The increase in nutrient input due to an increased weathering flux under the warm hyperthermal climate may have triggered the proliferation of marine vertebrates at Site 762C. However, at Sites 752 and 738C, there was no clear signature of BCP increase at H2, I1, or ETM3 (Yasukawa et al., 2017). Our results indicate that the prosperity of marine vertebrates may have sensitively responded to hyperthermals with significant regional variation, even within the Indian Ocean.

5.6.3 Post-Depositional Geochemical Processes Associated with Hyperthermals

The IC1, IC4, IC5, and IC6, which can be interpreted as post-depositional processes, showed multiple spike-like excursions at hyperthermal horizons (Figure 6b, c). As previously described, IC4 was interpreted as the diagenetic carbonate signature characterized by the positive correlation between Mn and $CaCO_3$. The depletion and reconcentration of Mn have been interpreted as diagenetic signatures associated with reduction and oxidation in the sediments (e.g., Burdige & Gieskies, 1983), the fluctuations of IC4 score at hyperthermal horizons can be interpreted as changes in the sediment redox condition.

As we discuss in Section 5.4.5., IC1, IC5, and IC6 were all characterized by redox-sensitive elements, which suggests changes in the redox condition of sediment pore water and/or bottom seawater. Still, they differed from IC4 because they have no clear correlation with $CaCO_3$ (Figure 4). IC1, IC5, and IC6 exhibited sharp peaks nearby hyperthermal horizons, and peaks tend to shift slightly between each IC (Figure 6b, c). At the horizon of the PETM-onset, there was a positive excursion of IC5 at the onset of CIE and peaks of IC1 and IC6 above the Hiatus D (Figure 6c). Therefore, we suggest that these ICs capture the enrichment and dissolution of redox-sensitive elements in the PETM layer of Site 762C. At the horizon of I1, IC1 peaks near the CIE level, and IC5 and IC6 peak above and below the CIE (Figure 6b). Such obvious excursions of IC score peaks occurring nearby hyperthermals are also observed in the H2, J, and ETM3 horizons, suggesting the occurrence of elemental enrichment and dissolution

systematically occurred at the hyperthermal events. However, there may be variations in the magnitude of redox-change in each event.

The reductive horizons in Site 762C identified through ICA may indicate that the redox state of the porewater and bottom water at the Exmouth Plateau in the Eastern Indian Ocean fluctuated during hyperthermals. Regarding the PETM, previous studies have reported that the enrichment and dissolution of redox-sensitive elements indicate that the redox state of the bottom water became reductive (~suboxic) at several sites in the Atlantic and Indian Oceans (Chun et al., 2010; Pälike et al., 2014). Our results are consistent with these previous studies, suggesting that porewater or bottom-water redox changes occurred in the mid-latitude eastern Indian Ocean. Furthermore, our data indicate novel insights into repetitive redox changes associated with the modest, multiple hyperthermals after the PETM. In addition, Zhou et al. (2014) suggested the occurrence of upper ocean deoxygenation during the PETM based on I/Ca record of bulk carbonate sediments from each ocean basin, including Site 762C. Therefore, the redox condition in hyperthermal horizons of Site 762C sediments is potentially linked to the upper ocean dissolved oxygen concentration and primary production rate at the photic zone.

5.7. Insights into Decoding the Paleoenvironmental Changes in Hyperthermals with ICA

Our study sheds light on the complex interplay between transient global warmings (i.e., hyperthermals) and paleoceanographic responses. As we noted in Section 3.5., the ICs extracted from the bulk chemical composition were statistically independent. In other words, each IC reflected a signature imprinted in sediments that can be considered a distinct geochemical feature. In reconstructing the paleoceanographic record at Site 762C, each IC can be interpreted as a reflection of a distinct aspect of paleoenvironmental changes due to the hyperthermals. Under the warm hyperthermal climate, increased chemical weathering and riverine drainage could have occurred (e.g., Dickson et al., 2015; Pogge von Strandmann et al., 2021; Ravizza et al., 2001; Tanaka et al., 2022). The increase in the relative contribution of the fluvial detrital component, represented by positive excursions in IC3, can be interpreted as a result of these environmental changes. Additionally, increased continental runoff may have also caused a significant input of nutrients to the continental margin. Given that Site 762C is located on the northwestern margin of offshore Australia, this increase in nutrient supply could have enhanced the marine primary productivity around the site. The positive excursions of IC2, which indicate an increase of BCP accumulation at hyperthermal horizons, suggest another vestige of the warming events from a biological/ecological perspective.

The results of ICA also indicate the impact of hyperthermals on seawater chemistry. During hyperthermals, at least locally/regionally, oceans are thought to have stratified due to warming (e.g., Sluijs et al., 2009; Tripati & Elderfield, 2005; Willard et al., 2019; Zachos et al., 2003). Furthermore, although regional variations may have existed, bottom seawater is considered to have become hypoxic–suboxic (e.g., Kaiho et al., 2006; Pälike et al., 2014; Papadomanolaki et al., 2022; Zhou et al., 2016). Excessive sedimentation of organic matter due to the increased nutrient supply from land and high productivity in the surface ocean may have induced bottom-water hypoxia on the continental shelf owing to enhanced oxygen consumption (Sluijs et al., 2014), as well as decreased dissolved oxygen due to high water temperatures associated with hyperthermals. Such environmental changes during hyperthermals could have resulted in changes in the redox state at the sediment–water interface and the uppermost

sediment. This process could have mobilized several redox-sensitive elements after deposition and caused the pyrite precipitation in the reductive zone. Depending on the differences in the kinetics and chemical affinity of each element, redistribution and enrichment of different sets of elements might have occurred in the sediment. These distinct features were subsequently separated as IC1, IC4, IC5, and IC6, which are mutually superimposed as statistically independent data structures in the sediment. Overall, the result of ICA on the bulk chemical composition of Site 762C sediments provides insights into various paleoceanographic processes during hyperthermals; each independent signature of multi-elemental geochemistry reflects different aspects of the effects of global warming on terrestrial and marine environments.

Since our study is based on the bulk chemical composition, our discussion remains limited to suggesting the geological phenomena that result in the accumulation and migration of source materials at this site. To further validate these interpretations, future investigations using proxies for continental chemical weathering (e.g., $^{187}Os/^{188}Os$ and $\delta^{7}Li$; Pogge von Strandmann et al., 2021; Ravizza et al., 2001; Tanaka et al., 2022), biological productivity (e.g., barite accumulation rate and $\delta^{138/134}Ba$; Bains et al., 2000; Bridgestock et al., 2019; Ma et al., 2014; Miyazaki et al., 2023), paleo-seawater pH (e.g., $\delta^{11}B$; Anagnostou et al., 2020; Gutjahr et al., 2017; Harper et al., 2020; Henehan et al., 2020), and paleo-redox conditions (e.g., $\delta^{98/95}Mo$ and $\delta^{15}N$; Auderset et al., 2022; Dickson, 2017; Siebert et al., 2003) may be necessary. By combining the results of ICA applied to bulk chemistry with a multi-proxy record involving various isotopes, we expect to gain a deeper understanding of the Earth system's responses to transient global warmings during the early Paleogene.

6 Conclusions

We newly reported $\delta^{13}C$, $\delta^{18}O$, and the chemical composition of bulk carbonate sediments at ODP Site 762C on the Exmouth Plateau in the eastern Indian Ocean and identified the long-term climatic trend (i.e., the EECO followed by the cooling) and five transient hyperthermals (i.e., PETM (onset), H2, I1, J, and ETM3). Through the ICA on the bulk chemical compositions, we extracted six ICs, including ICs representing the mixing relation between biogenic $CaCO_3$ and detrital material (IC3), biogenic calcium phosphate (IC2), diagenetic processes involving Mn-carbonate (IC4), and post-depositional remobilization of redox-sensitive elements (IC1, IC5, IC6) associated with diagenesis and changes in redox conditions. The decrease in IC3 scores during 55–52 Ma suggests a decrease in the contribution of biogenic $CaCO_3$ or an increase in the riverine terrigenous input relating to significant oceanographic and terrestrial environmental changes in the Early Eocene. Additionally, negative excursions in IC3 scores were observed during hyperthermals, indicating CCD shallowing or an increase of detrital input due to enhanced continental weathering during these events. IC2 scores, which reflect the contribution of BCP, indicate the proliferation of marine vertebrates at hyperthermals. IC1, IC4, IC5, and IC6, characterized by redox-sensitive elements, show peaks around the hyperthermals. This feature suggests that changes in the redox state of porewater or bottom water occurred associated with hyperthermals at Site 762C. Through our study, we shed light on the behaviors of biological and oceanographic responses of mid-latitude eastern Indian Ocean on early Paleogene climate changes.

Acknowledgments

This research was funded by the Japan Society for Promotion of Science (JSPS) KAKENHI Grants No. 20H05658 to Y. Kato, No. 17H01361 to K.N., No. 20H02678 to K.Y., and No. 20J22396 and 23K19025 to Y. Kuwahara. This study was performed under the cooperative research program of Center for Advanced Marine Core Research (present Marine Core Research Institute), Kochi University Accept No. 21A019 and 21B018 to Y. Kuwahara. This research used samples provided by the International Ocean Discovery Program (IODP). We appreciate Y. Kubo, IODP Curator at Kochi Core Center, for his invaluable support in sampling. We appreciate the support of Y. Itabashi, The University of Tokyo, with bulk chemical analyses. We are grateful to N. Fujimura and N. Shibuya at Kochi University, for their analytical support in stable isotope analyses.

Open Research

The R script for implementing ICA (fastICA algorithm) used in this study was originally composed and published by Yasukawa et al. (2023) and is available at https://doi.org/10.5281/zenodo.8098551

References

Algeo, T. J., & Maynard, J. B. (2004). Trace-element behavior and redox facies in core shales of Upper Pennsylvanian Kansas-type cyclothems. *Chemical Geology*, *206*(3–4), 289–318. https://doi.org/10.1016/j.chemgeo.2003.12.009

Alibo, D. S., & Nozaki, Y. (1999). Rare earth elements in seawater: Particle association, shale-normalization, and Ce oxidation. *Geochimica et Cosmochimica Acta*, *63*, (3–4). https://doi.org/10.1016/S0016-7037(98)00279-8

Anagnostou, E., John, E. H., Babila, T. L., Sexton, P. F., Ridgwell, A., & Lunt, D. J. (2020). Proxy evidence for state-dependence of climate sensitivity in the Eocene greenhouse. *Nature Communications*, *11*(1), 4436. https://doi.org/10.1038/s41467-020-17887-x

Anagnostou, E., John, E. H., Edgar, K. M., Foster, G. L., Ridgwell, A., Inglis, G. N., Pancost, R. D., Lunt, D. J., & Pearson, P. N. (2016). Changing atmospheric CO_2 concentration was the primary driver of early Cenozoic climate. *Nature*, *533*(7603), 380–384. https://doi.org/10.1038/nature17423

Assonov, S., Groening, M., Fajgelj, A., Hélie, J. F., & Hillaire-Marcel, C. (2020). Preparation and characterisation of IAEA-603, a new primary reference material aimed at the VPDB scale realisation for $\delta^{13}C$ and $\delta^{18}O$ determination. *Rapid Communications in Mass Spectrometry*, *34*(20). https://doi.org/10.1002/rcm.8867

Auderset, A., Moretti, S., Taphorn, B., Ebner, P.-R., Kast, E., Wang, X. T., Schiebel, R., Sigman, D. M., Haug, G. H., & Martínez-García, A. (2022). Enhanced ocean oxygenation during Cenozoic warm periods. *Nature*, *609*(7925), 77–82. https://doi.org/10.1038/s41586-022-05017-0

Bains, S., Norris, R. D., Corfield, R. M., & Faul, K. L. (2000). Termination of global warmth at the Palaeocene/Eocene boundary through productivity feedback. *Nature*, *407*(6801), 171–174. https://doi.org/10.1038/35025035

Barnet, J. S. K., Littler, K., Westerhold, T., Kroon, D., Leng, M. J., Bailey, I., Röhl, U., & Zachos, J. C. (2019). A High-Fidelity Benthic Stable Isotope Record of Late Cretaceous–Early Eocene Climate Change and Carbon-Cycling. *Paleoceanography and Paleoclimatology*, *34*(4), 672–691. https://doi.org/10.1029/2019PA003556

Barras, C., Mouret, A., Nardelli, M. P., Metzger, E., Petersen, J., La, C., Filipsson, H. L., & Jorissen, F. (2018). Experimental calibration of manganese incorporation in foraminiferal calcite. *Geochimica et Cosmochimica Acta*, *237*, 49–64. https://doi.org/10.1016/j.gca.2018.06.009

Bilal, A., & McClay, K. (2022). Tectonic and stratigraphic evolution of the central Exmouth Plateau, NW Shelf of Australia. *Marine and Petroleum Geology*, *136*, 105447. https://doi.org/10.1016/j.marpetgeo.2021.105447

Bolhar, R., Kamber, B. S., Moorbath, S., Fedo, C. M., & Whitehouse, M. J. (2004). Characterisation of early Archaean chemical sediments by trace element signatures. *Earth and Planetary Science Letters*, *222*(1), 43–60. https://doi.org/10.1016/j.epsl.2004.02.016

Boyle, E. A. (1983). Manganese carbonate overgrowths on foraminifera tests. *Geochimica et Cosmochimica Acta*, *47*(10), 1815–1819. https://doi.org/10.1016/0016-7037(83)90029-7

Bralower, T. J. (2002). Evidence of surface water oligotrophy during the Paleocene-Eocene thermal maximum: Nannofossil assemblage data from Ocean Drilling Program Site 690, Maud Rise, Weddell Sea. *Paleoceanography*, *17*(2), 1023. https://doi.org/10.1029/2001pa000662

Bridgestock, L., Hsieh, Y., Porcelli, D., & Henderson, G. M. (2019). Increased export production during recovery from the Paleocene–Eocene thermal maximum constrained by sedimentary Ba isotopes. *Earth and Planetary Science Letters*, *510*, 53–63. https://doi.org/10.1016/j.epsl.2018.12.036

Britten, G. L., & Sibert, E. C. (2020). Enhanced fish production during a period of extreme global warmth. *Nature Communications*, *11*(1), 5636. https://doi.org/10.1038/s41467-020-19462-w

Burdige, D. J., & Gieskes, J. M. (1983). A pore water/solid phase diagenetic model for manganese in marine sediments. *American Journal of Science*, *283*(1), 29–47. https://doi.org/10.2475/ajs.283.1.29

Burton, Z. F. M., McHargue, T., Kremer, C. H., Bloch, R. B., Gooley, J. T., Jaikla, C., Harrington, J., & Graham, S. A. (2023). Peak Cenozoic warmth enabled deep-sea sand deposition. *Scientific Reports*, *13*(1), 1276. https://doi.org/10.1038/s41598-022-27138-2

Calvert, S. E., & Pedersen, T. F. (1993). Geochemistry of Recent oxic and anoxic marine sediments: Implications for the geological record. *Marine Geology*, *113*(1–2), 67–88. https://doi.org/10.1016/0025-3227(93)90150-T

Charisi, S. D., & Schmitz, B. (1996). Early Eocene palaeoceanography and palaeoclimatology of the eastern North Atlantic: stable isotope results for DSDP Hole 550. *Geological Society, London, Special Publications*, *101*(1), 457–472. https://doi.org/10.1144/GSL.SP.1996.101.01.22

Chun, C. O. J., Delaney, M. L., & Zachos, J. C. (2010). Paleoredox changes across the Paleocene-Eocene thermal maximum, Walvis Ridge (ODP Sites 1262, 1263, and 1266): Evidence from Mn and U enrichment factors. *Paleoceanography*, *25*(4), 1–13. https://doi.org/10.1029/2009PA001861

Cramer, B. S., Wright, J. D., Kent, D. V., & Aubry, M. P. (2003). Orbital climate forcing of $\delta^{13}C$ excursions in the late Paleocene-early Eocene (chrons C24n-C25n). *Paleoceanography*, *18*(4), 1097. https://doi.org/10.1029/2003PA000909

Dallanave, E., Agnini, C., Bachtadse, V., Muttoni, G., Crampton, J. S., Percy Strong, C., Hines, B. R., Hollis, C. J., & Slotnick, B. S. (2015). Early to middle Eocene magneto-biochronology of the southwest Pacific Ocean and climate influence on sedimentation: Insights from the Mead Stream section, New Zealand. *Bulletin of the Geological Society of America*, *127*(5–6), 643–660. https://doi.org/10.1130/B31147.1

De Baar, H. J. W., Bacon, M. P., Brewer, P. G., & Bruland, K. W. (1985). Rare earth elements in the Pacific and Atlantic Oceans. *Geochimica et Cosmochimica Acta*, *49*(9), 1943–1959. https://doi.org/10.1016/0016-7037(85)90089-4

Dickson, A. J. (2017). A molybdenum-isotope perspective on Phanerozoic deoxygenation events. *Nature Geoscience*, *10*(10), 721–726. https://doi.org/10.1038/NGEO3028

Dickson, A. J., Cohen, A. S., Coe, A. L., Davies, M., Shcherbinina, E. A., & Gavrilov, Y. O. (2015). Evidence for weathering and volcanism during the PETM from Arctic Ocean and Peri-Tethys osmium isotope records. *Palaeogeography, Palaeoclimatology, Palaeoecology*, *438*, 300–307. https://doi.org/10.1016/j.palaeo.2015.08.019

Dunlea, A. G., Murray, R. W., Sauvage, J., Spivack, A. J., Harris, R. N., & D'Hondt, S. (2015). Dust, volcanic ash, and the evolution of the South Pacific Gyre through the Cenozoic. *Paleoceanography*, *30*(8), 1078–1099. https://doi.org/10.1002/2015PA002829

Dutton, A., Lohmann, K. C., & Leckie, R. M. (2005). Insights from the Paleogene tropical Pacific: Foraminiferal stable isotope and elemental results from Site 1209, Shatsky Rise. *Paleoceanography*, *20*(3), PA3004. https://doi.org/10.1029/2004PA001098

Galbrun, B. (1992). Magnetostratigraphy of Upper Cretaceous and Lower Tertiary sediments, Sites 761 and 762, Exmouth Plateau, northwest Australia. *Proc. Scientific Results, ODP, Leg 122, Exmouth Plateau*, *122*, 699–716. https://doi.org/10.2973/odp.proc.sr.122.149.1992

Gibbs, S. J., Bralower, T. J., Bown, P. R., Zachos, J. C., & Bybell, L. M. (2006). Shelf and open-ocean calcareous phytoplankton assemblages across the Paleocene-Eocene thermal maximum: Implications for global productivity gradients. *Geology*, *34*(4), 233–236. https://doi.org/10.1130/G22381.1

Gutjahr, M., Ridgwell, A., Sexton, P. F., Anagnostou, E., Pearson, P. N., Pälike, H., Norris, R. D., Thomas, E., & Foster, G. L. (2017). Very large release of mostly volcanic carbon during the Palaeocene-Eocene Thermal Maximum. *Nature*, *548*(7669), 573–577. https://doi.org/10.1038/nature2364

Guttman, L. (1954), Some necessary conditions for common factor analysis. *Psychometrika*, *19*, 149–161. https://doi.org/10.1007/BF02289162

Hancock, H. J. L., Chaproniere, G. C., Dickens, G. R., & Henderson, R. A. (2002). Early Palaeogene planktic foraminiferal and carbon isotope stratigraphy, Hole 762C, Exmouth Plateau, northwest Australian margin. *Journal of Micropalaeontology*, *21*(1), 29–42. https://doi.org/10.1144/jm.21.1.29

Haq, B. U., Boyd, R. L., Exon, N. F., & Von Rad, U. (1992). Evolution of the central Exmouth Plateau: a post-drilling perspective. In *Proceedings of the Ocean Drilling Program, Scientific Results* (Vol. 122, pp. 801–816). College Station, TX: Ocean Drilling Program. https://doi.org/10.2973/odp.proc.sr.122.182.1992

Haq, B. U., von Rad, U. & O'Connell, S. (1990). Site 762. *In* Haq, B. U., von Rad, U. & O'Connell. S. *Proceedings of the ocean drilling program, Initial Reports, Leg 122*, (Vol. 122, pp. 213–288). College Station, TX: Ocean Drilling Program. https://doi.org/10.2973/odp.proc.ir.122.108.1990

Harper, D. T., Hönisch, B., Zeebe, R. E., Shaffer, G., Haynes, L. L., Thomas, E., & Zachos, J. C. (2020). The Magnitude of Surface Ocean Acidification and Carbon Release During Eocene Thermal Maximum 2 (ETM-2) and the Paleocene-Eocene Thermal Maximum (PETM). *Paleoceanography and Paleoclimatology*, *35*(2), e2019PA003699. https://doi.org/10.1029/2019PA003699

Henehan, M. J., Edgar, K. M., Foster, G. L., Penman, D. E., Hull, P. M., Greenop, R., Anagnostou, E., & Pearson, P. N. (2020). Revisiting the Middle Eocene Climatic Optimum "Carbon Cycle Conundrum" With New Estimates of Atmospheric pCO_2 From Boron Isotopes. *Paleoceanography and Paleoclimatology*, *35*(6), e2019PA003713. https://doi.org/10.1029/2019PA003713

Hollis, C. J., Hines, B. R., Littler, K., Villasante-Marcos, V., Kulhanek, D. K., Strong, C. P., Zachos, J. C., Eggins, S. M., Northcote, L., & Phillips, A. (2015). The Paleocene-Eocene Thermal Maximum at DSDP Site 277, Campbell Plateau, southern Pacific Ocean. *Climate of the Past*, *11*(7), 1009–1025. https://doi.org/10.5194/cp-11-1009-2015

Huerta-Diaz, M. A., & Morse, J. W. (1992). Pyritization of trace metals in anoxic marine sediments. *Geochimica et Cosmochimica Acta*, *56*(7), 2681–2702. https://doi.org/10.1016/0016-7037(92)90353-K

Hyland, E. G., & Sheldon, N. D. (2013). Coupled CO_2-climate response during the Early Eocene Climatic Optimum. *Palaeogeography, Palaeoclimatology, Palaeoecology*, *369*, 125–135. https://doi.org/10.1016/j.palaeo.2012.10.011

Hyland, E. G., Sheldon, N. D., & Cotton, J. M. (2017). Constraining the early Eocene climatic optimum: A terrestrial interhemispheric comparison. *Bulletin of the Geological Society of America*, *129*(1–2), 244–252. https://doi.org/10.1130/B31493.1

Imai, N., Terashima, S., Itoh, S., & Ando, A. (1995). 1994 Compilation of analytical data for minor and trace elements in seventeen GSJ geochemical reference samples, "Igneous rock series." *Geostandards and Geoanalytical Research*, *19*(2), 135–213. https://doi.org/10.1111/j.1751-908X.1995.tb00158.x

Ishizuka, O., Tani, K., Reagan, M. K., Kanayama, K., Umino, S., Harigane, Y., Sakamoto, I., Miyajima, Y., Yuasa, M., & Dunkley, D. J. (2011). The timescales of subduction initiation and subsequent evolution of an oceanic island arc. *Earth and Planetary Science Letters*, *306*(3–4), 229–240. https://doi.org/10.1016/j.epsl.2011.04.006

Iwamori, H., & Albarède, F. (2008). Decoupled isotopic record of ridge and subduction zone processes in oceanic basalts by independent component analysis. *Geochemistry, Geophysics, Geosystems*, *9*(4), Q04033. https://doi.org/10.1029/2007GC001753

Jones, R. W., & Wonders, A. A. H. (1992). Benthic foraminifers and paleobathymetry of Barrow Group (Berriasian-Valanginian) deltaic sequences, Sites 762 and 763, Northwest Shelf, Australia. *Proc. Scientific Results, ODP, Leg 122, Exmouth Plateau*, *122*, 557–568. https://doi.org/10.2973/odp.proc.sr.122.174.1992

Kaiho, K., Takeda, K., Petrizzo, M. R., & Zachos, J. C. (2006). Anomalous shifts in tropical Pacific planktonic and benthic foraminiferal test size during the Paleocene-Eocene thermal maximum. *Palaeogeography, Palaeoclimatology, Palaeoecology*, *237*(2–4), 456–464. https://doi.org/10.1016/j.palaeo.2005.12.017

Kaiser, H. F. (1960). The application of electronic computers to factor analysis. Educational and *Psychological Measurement*, 20, 141–151. https://doi.org/10.1177/001316446002000116

Kashiwabara, T., Toda, R., Fujinaga, K., Honma, T., Takahashi, Y., & Kato, Y. (2014). Determination of host phase of lanthanum in deep-sea REY-rich mud by XAFS and μ-XRF using high-energy synchrotron radiation. *Chemistry Letters*, *43*(2), 199–200. https://doi.org/10.1246/cl.130853

Kato, Y., Fujinaga, K., Nakamura, K., Takaya, Y., Kitamura, K., Ohta, J., Toda, R., Nakashima, T., & Iwamori, H. (2011). Deep-sea mud in the Pacific Ocean as a potential resource for rare-earth elements. *Nature Geoscience*, *4*(8), 535–539. https://doi.org/10.1038/ngeo1185

Kato, Y., Fujinaga, K., & Suzuki, K. (2005). Major and trace element geochemistry and Os isotopic composition of metalliferous umbers from the Late Cretaceous Japanese accretionary complex. *Geochemistry, Geophysics, Geosystems*, *6*(7), Q07004. https://doi.org/10.1029/2005GC000920

Kennett, P., & Stott, D. (1991). Abrupt deep-sea warming, palaeoceanographic changes and benthic extinctions at the end of the Palaeocene. *Nature*, *353*, 225–229.

Kirtland Turner, S., Sexton, P. F., Charles, C. D., & Norris, R. D. (2014). Persistence of carbon release events through the peak of early Eocene global warmth. *Nature Geoscience*, *7*(10), 748–751. https://doi.org/10.1038/NGEO2240

Komar, N., Zeebe, R. E., & Dickens, G. R. (2013). Understanding long-term carbon cycle trends: The late Paleocene through the early Eocene. *Paleoceanography*, *28*(4), 650–662. https://doi.org/10.1002/palo.20060

Lauretano, V., Littler, K., Polling, M., Zachos, J. C., & Lourens, L. J. (2015). Frequency, magnitude and character of hyperthermal events at the onset of the Early Eocene Climatic Optimum. *Climate of the Past*, *11*(10), 1313–1324. https://doi.org/10.5194/cp-11-1313-2015

Leon-Rodriguez, L., & Dickens, G. R. (2010). Constraints on ocean acidification associated with rapid and massive carbon injections: The early Paleogene record at ocean drilling program site 1215, equatorial Pacific Ocean. *Palaeogeography, Palaeoclimatology, Palaeoecology*, *298*(3–4), 409–420. https://doi.org/10.1016/j.palaeo.2010.10.029

Littler, K., Röhl, U., Westerhold, T., & Zachos, J. C. (2014). A high-resolution benthic stable-isotope record for the South Atlantic: Implications for orbital-scale changes in Late Paleocene-Early Eocene climate and carbon cycling. *Earth and Planetary Science Letters*, *401*, 18–30. https://doi.org/10.1016/j.epsl.2014.05.054

Lourens, L. J., Sluijs, A., Kroon, D., Zachos, J. C., Thomas, E., Röhl, U., Bowles, J., & Raffi, I. (2005). Astronomical pacing of late Palaeocene to early Eocene global warming events. *Nature*, *435*(7045), 1083–1087. https://doi.org/10.1038/nature03814

Lu, Y., Makishima, A., & Nakamura, E. (2007). Coprecipitation of Ti, Mo, Sn and Sb with fluorides and application to determination of B, Ti, Zr, Nb, Mo, Sn, Sb, Hf and Ta by ICP-MS. *Chemical Geology*, *236*(1–2), 13–26. https://doi.org/10.1016/j.chemgeo.2006.08.007

Luciani, V., D'Onofrio, R., Dickens, G. R., & Wade, B. S. (2017). Planktic foraminiferal response to early Eocene carbon cycle perturbations in the southeast Atlantic Ocean (ODP Site 1263). *Global and Planetary Change*, *158*, 119–133. https://doi.org/10.1016/j.gloplacha.2017.09.007

Luciani, V., R Dickens, G., Backman, J., Fornaciari, E., Giusberti, L., Agnini, C., & D'Onofrio, R. (2016). Major perturbations in the global carbon cycle and photosymbiont-bearing planktic foraminifera during the early Eocene. *Climate of the Past*, *12*(4), 981–1007. https://doi.org/10.5194/cp-12-981-2016

Ma, Z., Gray, E., Thomas, E., Murphy, B., Zachos, J., & Paytan, A. (2014). Carbon sequestration during the Palaeocene-Eocene Thermal Maximum by an efficient biological pump. *Nature Geoscience*, *7*(5), 382–388. https://doi.org/10.1038/ngeo2139

Makishima, A., & Nakamura, E. (2006). Determination of Major/ Minor and Trace Elements in Silicate Samples by ICP-QMS and ICP-SFMS Applying Isotope Dilution-Internal Standardisation (ID-IS) and Multi-Stage Internal Standardisation. *Geostandards and Geoanalytical Research*, *30*(3), 245–271. https://doi.org/10.1111/j.1751-908X.2006.tb01066.x

Marchini, J. L., Heaton, C., & Ripley, B. D. (2013). Package 'fastICA' Reference manual. Retrieved from http://cran.r-project.org/web/packages/fastICA/index.html

Martini, E. (1971). Standard Tertiary and Quaternary calcareous nannoplankton zonation. *In* Farinacci, A., ed., *Proceedings of the Second Planktonic Conference Roma 1970*, Tecnoscienza, Roma, 739–785.

McInerney, F. A., & Wing, S. L. (2011). The paleocene-eocene thermal maximum: A perturbation of carbon cycle, climate, and biosphere with implications for the future. *Annual Review of Earth and Planetary Sciences*, *39*, 489–516. https://doi.org/10.1146/annurev-earth-040610-133431

Miyazaki, T., Yasukawa, K., Tanaka, E., Vaglarov, B. S., & Yoshida, K. (2023). Ba stable isotope excursions induced by multiple hyperthermal events: A potential new index for transient global warming. *Geochemical Journal 57*(4), e1–e8. https://doi.org/10.2343/geochemj.gj23011

Murray, R. W., Buchholtz Ten Brink, M. R., Gerlach, D. C., Russ, G. P., & Jones, D. L. (1991). Rare earth, major, and trace elements in chert from the Franciscan Complex and Monterey Group, California: Assessing REE sources to fine-grained marine sediments. *Geochimica et Cosmochimica Acta*, *55*(7), 1875–1895. https://doi.org/10.1016/0016-7037(91)90030-9

Nicolo, M. J., Dickens, G. R., Hollis, C. J., & Zachos, J. C. (2007). Multiple early Eocene hyperthermals: Their sedimentary expression on the New Zealand continental margin and in the deep sea. *Geology*, *35*(8), 699–702. https://doi.org/10.1130/G23648A.1

O'Connor, J. M., Steinberger, B., Regelous, M., Koppers, A. A. P., Wijbrans, J. R., Haase, K. M., Stoffers, P., Jokat, W., & Garbe-Schönberg, D. (2013). Constraints on past plate and mantle motion from new ages for the Hawaiian-Emperor Seamount Chain. *Geochemistry, Geophysics, Geosystems*, *14*(10), 4564–4584. https://doi.org/10.1002/ggge.20267

Okada, H., & Bukry, D. (1980). Supplementary modification and introduction of code numbers to the low-latitude coccolith biostratigraphic zonation (Bukry, 1973; 1975). *Marine Micropaleontology*, *5*(3), 321–325.

Pälike, C., Delaney, M. L., & Zachos, J. C. (2014). Deep-sea redox across the Paleocene-Eocene thermal maximum. *Geochemistry, Geophysics, Geosystems*, *15*, 1038–1053. https://doi.org/10.1002/2013GC005074.Received

Pälike, H., Lyle, M. W., Nishi, H., Raffi, I., Ridgwell, A., Gamage, K., Klaus, A., Acton, G. et al. (2012). A Cenozoic record of the equatorial Pacific carbonate compensation depth. *Nature*, *488*(7413), 609–614. https://doi.org/10.1038/nature11360

Papadomanolaki, N. M., Sluijs, A., & Slomp, C. P. (2022). Eutrophication and Deoxygenation Forcing of Marginal Marine Organic Carbon Burial During the PETM. *Paleoceanography and Paleoclimatology*, *37*(3). https://doi.org/10.1029/2021PA004232

Plank, T., & Langmuir, C. H. (1998). The chemical composition of subducting sediment and its consequences for the crust and mantle. *Chemical Geology*, *145*(3–4), 325–394. https://doi.org/10.1016/S0009-2541(97)00150-2

Pogge von Strandmann, P. A. E., Jones, M. T., Joshua West, A., Murphy, M. J., Stokke, E. W., Tarbuck, G., Wilson, D. J., Pearce, C. R., & Schmidt, D. N. (2021). Lithium isotope evidence for enhanced weathering and erosion during the Paleocene-Eocene Thermal Maximum. *Science Advances*, *7*(42), eabh4224. https://doi.org/10.1126/sciadv.abh4224

Raffi, I., & De Bernardi, B. (2008). Response of calcareous nannofossils to the Paleocene-Eocene Thermal Maximum: Observations on composition, preservation and calcification in sediments from ODP Site 1263 (Walvis Ridge - SW Atlantic). *Marine Micropaleontology*, *69*(2), 119–138. https://doi.org/10.1016/j.marmicro.2008.07.002

Ravizza, G. E., & Zachos, J. C. (2014). Records of Cenozoic Ocean Chemistry. In *Treatise on Geochemistry: Second Edition* (Vol. 8, pp. 543–568). Elsevier Inc. https://doi.org/10.1016/B978-0-08-095975-7.00620-3

Ravizza, G., Norris, R. N., Blusztajn, J., & Aubry, M. P. (2001). An osmium isotope excursion associated with the late Paleocene thermal maximum: Evidence of intensified chemical weathering. *Paleoceanography*, *16*(2), 155–163. https://doi.org/10.1029/2000PA000541

Reichgelt, T., Greenwood, D. R., Steinig, S., Conran, J. G., Hutchinson, D. K., Lunt, D. J., Scriven, L. J., & Zhu, J. (2022). Plant Proxy Evidence for High Rainfall and Productivity in the Eocene of Australia. *Paleoceanography and Paleoclimatology*, *37*(6), e2022PA004418. https://doi.org/10.1029/2022PA004418

Rudnick, R. L., & Gao, S. (2014). Composition of the Continental Crust. In *Treatise on Geochemistry: Second Edition* (Vol. 4, pp. 1–51). Elsevier Inc. https://doi.org/10.1016/B978-0-08-095975-7.00301-6

Scotese, C. R. (2001). Atlas of Earth history. PALEOMAP Project.

Shamrock, J. L., & Watkins, D. K. (2012). Eocene calcareous nannofossil biostratigraphy and community structure from Exmouth Plateau, Eastern Indian Ocean (ODP Site 762). *Stratigraphy*, *9*(1), 1–54.

Shamrock, J. L., Watkins, D. K., & Johnston K. W. (2012). Eocene biogeochronology and magnetostratigraphic revision of ODP Hole 762C, Exmouth Plateau (northwest Australian Shelf). *Stratigraphy 9*(1): 55-75.

Sibert, E., Norris, R., Cuevas, J., & Graves, L. (2016). Eighty-five million years of Pacific Ocean gyre ecosystem structure: Long-term stability marked by punctuated change. *Proceedings of the Royal Society B: Biological Sciences*, *283*(1831). https://doi.org/10.1098/rspb.2016.0189

Siebert, C., Nägler, T. F., von Blanckenburg, F., & Kramers, J. D. (2003). Molybdenum isotope records as a potential new proxy for paleoceanography. *Earth and Planetary Science Letters*, *211*(1–2), 159–171. https://doi.org/10.1016/S0012-821X(03)00189-4

Slotnick, B. S., Lauretano, V., Backman, J., Dickens, G. R., Sluijs, A., & Lourens, L. (2015). Early Paleogene variations in the calcite compensation depth: New constraints using old borehole sediments from across Ninetyeast Ridge, central Indian Ocean. *Climate of the Past*, *11*(3), 473–493. https://doi.org/10.5194/cp-11-473-2015

Sluijs, A., Schouten, S., Donders, T. H., Schoon, P. L., Röhl, U., Reichart, G. J., Sangiorgi, F., Kim, J. H., Sinninghe Damsté, J. S., & Brinkhuis, H. (2009). Warm and wet conditions in the Arctic region during Eocene Thermal Maximum 2. *Nature Geoscience*, *2*(11), 777–780. https://doi.org/10.1038/ngeo668

Sluijs, A., Zeebe, R. E., Bijl, P. K., & Bohaty, S. M. (2013). A middle Eocene carbon cycle conundrum. *Nature Geoscience*, *6*(6), 429–434. https://doi.org/10.1038/ngeo1807

Speijer, R. P., Pälike, H., Hollis, C. J., Hooker, J. J., & Ogg, J. G. (2020). Chapter 28 - The Paleogene Period. In F. M. Gradstein, J. G. Ogg, M. D. Schmitz, & G. M. Ogg (Eds.), *Geologic Time Scale 2020* (pp. 1087–1140). Elsevier. https://doi.org/https://doi.org/10.1016/B978-0-12-824360-2.00028-0

Swanner, E. D., Webb, S. M., & Kappler, A. (2019). Fate of cobalt and nickel in mackinawite during diagenetic pyrite formation. *American Mineralogist*, *104*(7), 917–928. https://doi.org/10.2138/am-2019-6834

Takaya, Y., Yasukawa, K., Kawasaki, T., Fujinaga, K., Ohta, J., Usui, Y., Nakamura, K., Kimura, J. I., Chang, Q., Hamada, M., Dodbiba, G., Nozaki, T., Iijima, K., Morisawa, T., Kuwahara, T., Ishida, Y., Ichimura, T., Kitazume, M., Fujita, T., & Kato, Y. (2018). The tremendous potential of deep-sea mud as a source of rare-earth elements. *Scientific Reports*, *8*(1), 5763. https://doi.org/10.1038/s41598-018-23948-5

Tanaka, E., Yasukawa, K., Ohta, J., & Kato, Y. (2022). Enhanced continental chemical weathering during the multiple early Eocene hyperthermals: New constraints from the southern Indian Ocean. *Geochimica et Cosmochimica Acta*, *331*, 192–211. https://doi.org/10.1016/j.gca.2022.05.022

Thomas, D. J., Bralower, T. J., & Jones, C. E. (2003). Neodymium isotopic reconstruction of late Paleocene-early Eocene thermohaline circulation. *Earth and Planetary Science Letters*, *209*(3–4), 309–322. https://doi.org/10.1016/S0012-821X(03)00096-7

Thomas, E. (1998). Biogeography of the Late Paleocene benthic foraminiferal extinction. In *Late Paleocene-early Eocene biotic and climatic events in the marine and terrestrial records* (pp. 214–243). Columbia University Press.

Thomas, E., Shackleton, N. J., & Hall, M. A. (1992). Data Report: Carbon Isotope Stratigraphy of Paleogene Bulk Sediments, Hole 762C (Exmouth Plateau, Eastern Indian Ocean). In *Proceedings of the Ocean Drilling Program, Scientific Results* (Vol. 122, pp. 410–412). College Station, TX: Ocean Drilling Program. https://doi.org/10.2973/odp.proc.sr.122.195.1992

Thomson, J., Higgs, N. C., Croudace, I. W., Colley, S., & Hydes, D. J. (1993). Redox zonation of elements at an oxic/post-oxic boundary in deep-sea sediments. *Geochimica et Cosmochimica Acta*, *57*(3), 579–595. https://doi.org/10.1016/0016-7037(93)90369-8

Thomson, J., Higgs, N. C., Jarvis, I., Hydes, D. J., Colley, S., & Wilson, T. R. S. (1986). The behaviour of manganese in Atlantic carbonate sediments. *Geochimica et Cosmochimica Acta*, *50*(8), 1807–1818. https://doi.org/10.1016/0016-7037(86)90140-7

Toyoda, K. & Tokonami, M. (1990). Diffusion of rare-earth elements in fish teeth from deep-sea sediments. *Nature* 345, 607–609.

Tremolada, F., & Bralower, T. J. (2004). Nannofossil assemblage fluctuations during the Paleocene-Eocene Thermal Maximum at Sites 213 (Indian Ocean) and 401 (North Atlantic Ocean): Palaeoceanographic implications. *Marine Micropaleontology*, *52*(1–4), 107–116. https://doi.org/10.1016/j.marmicro.2004.04.002

Tripati, A., & Elderfield, H. (2005). Deep-Sea Temperature and Circulation Changes at the Paleocene-Eocene Thermal Maximum. *Science*, *308*(5730), 1894–1898. https://doi.org/10.1126/science.1109202

Wade, B. S., Pearson, P. N., Berggren, W. A., & Pälike, H. (2011). Review and revision of Cenozoic tropical planktonic foraminiferal biostratigraphy and calibration to the geomagnetic polarity and astronomical time scale. *Earth-Science Reviews*, *104*(1–3), 111–142. https://doi.org/10.1016/j.earscirev.2010.09.003

Westerhold, T., Marwan, N., Drury, A. J., Liebrand, D., Agnini, C., Anagnostou, E., Barnet, J. S. K. et al. (2020). An astronomically dated record of Earth's climate and its predictability over the last 66 million years. *Science*, *369*(6509), 1383–1388. https://doi.org/10.1126/SCIENCE.ABA6853

Westerhold, T., Röhl, U., Donner, B., & Zachos, J. C. (2018). Global Extent of Early Eocene Hyperthermal Events: A New Pacific Benthic Foraminiferal Isotope Record From Shatsky Rise (ODP Site 1209). *Paleoceanography and Paleoclimatology*, *33*(6), 626–642. https://doi.org/10.1029/2017PA003306

Westerhold, T., Röhl, U., Frederichs, T., Agnini, C., Raffi, I., Zachos, J. C., & Wilkens, R. H. (2017). Astronomical calibration of the Ypresian timescale: Implications for seafloor spreading rates and the chaotic behavior of the solar system? *Climate of the Past*, *13*(9), 1129–1152. https://doi.org/10.5194/cp-13-1129-2017

Whittaker, J. M., Müller, R. D., Leitchenkov, G., Stagg, H., Sdrolias, M., Gaina, C., & Goncharov, A. (2007). Major Australian-Antarctic plate reorganization at Hawaiian-Emperor bend time. *Science*, *318*(5847), 83–86. https://doi.org/10.1126/science.1143769

Willard, D. A., Donders, T. H., Reichgelt, T., Greenwood, D. R., Sangiorgi, F., Peterse, F., Nierop, K. G. J., Frieling, J., Schouten, S., & Sluijs, A. (2019). Arctic vegetation, temperature, and hydrology during Early Eocene transient global warming events. *Global and Planetary Change*, *178*(4), 139–152. https://doi.org/10.1016/j.gloplacha.2019.04.012

Winguth, A. M. E., Thomas, E., & Winguth, C. (2012). Global decline in ocean ventilation, oxygenation, and productivity during the Paleocene-Eocene Thermal Maximum: Implications for the benthic extinction. *Geology*, *40*(3), 263–266. https://doi.org/10.1130/G32529.1

Xu, K., De Vleeschouwer, D., Vahlenkamp, M., Yang, R., & Chen, H. (2021). Reconstructing Eocene Eastern Indian Ocean dynamics using ocean-drilling stratigraphic records. *Paleoceanography and Paleoclimatology*, *36*, e2020PA004116. https://doi.org/10.1029/2020pa004116

Yasukawa, K., Kino, S., Azami, K., Tanaka, E., Mimura, K., Ohta, J., Fujinaga, K., Nakamura, K., & Kato, Y. (2020). Geochemical features of Fe-Mn micronodules in deep-sea sediments of the western North Pacific Ocean: Potential for co-product metal extraction from REY-rich mud. *Ore Geology Reviews*, *127*, 103805. https://doi.org/10.1016/j.oregeorev.2020.103805

Yasukawa, K., Nakamura, K., Fujinaga, K., Ikehara, M., & Kato, Y. (2017). Earth system feedback statistically extracted from the Indian Ocean deep-sea sediments recording Eocene hyperthermals. *Scientific Reports*, *7*(1), 11304. https://doi.org/10.1038/s41598-017-11470-z

Yasukawa, K., Nakamura, K., Fujinaga, K., Iwamori, H., & Kato, Y. (2016). Tracking the spatiotemporal variations of statistically independent components involving enrichment of rare-earth elements in deep-sea sediments. In *Scientific Reports*, *6*(1), 29603. https://doi.org/10.1038/srep29603

Yasukawa, K., Ohta, J., Hamada, M., Chang, Q., Nakamura, H., Ashida, K., Takaya, Y., Nakamura, K., Iwamori, H., & Kato, Y. (2022). Essential processes involving REE-enrichment in biogenic apatite in deep-sea sediment decoded via multivariate statistical analyses. *Chemical Geology*, *614*, 121184. https://doi.org/10.1016/j.chemgeo.2022.121184

Yasukawa, K., Ohta, J., Miyazaki, T., Vaglarov, B. S., Chang, Q., Ueki, K., Toyama, C., Kimura, J. I., Tanaka, E., Nakamura, K., Fujinaga, K., Iijima, K., Iwamori, H., & Kato, Y. (2019). Statistic and Isotopic Characterization of Deep-Sea Sediments in the Western North Pacific Ocean: Implications for Genesis of the Sediment Extremely Enriched in Rare Earth Elements. *Geochemistry, Geophysics, Geosystems*, *20*(7), 3402–3430. https://doi.org/10.1029/2019GC008214

Yasukawa, K., Tanaka, E., Miyazaki, T., Vaglarov, B. S., Chang, Q., Nakamura, K., Ohta, J., Fujinaga, K., Iwamori, H., & Kato, Y. (2023). R script for k-means cluster analysis with whitening and projection pursuit for a chemical composition dataset of pelagic clay around Minamitorishima Island in the western North Pacific Ocean. *Zenodo*. https://doi.org/10.5281/zenodo.8098551

Zachos, J. C., McCarren, H., Murphy, B., Röhl, U., & Westerhold, T. (2010). Tempo and scale of late Paleocene and early Eocene carbon isotope cycles: Implications for the origin of hyperthermals. *Earth and Planetary Science Letters*, *299*(1–2), 242–249. https://doi.org/10.1016/j.epsl.2010.09.004

Zachos, J. C., Röhl, U., Schellenberg, S. A., Sluijs, A., Hodell, D. A., Kelly, D. C., Thomas, E., Nicolo, M., Raffi, I., Lourens, L. J., McCarren, H., & Kroon, D. (2005). Paleoclimate: Rapid acidification of the ocean during the paleocene-eocene thermal maximum. *Science*, *308*(5728), 1611–1615. https://doi.org/10.1126/science.1109004

Zachos, J. C., Wara, M. W., Bohaty, S., Delaney, M. L., Petrizzo, M. R., Brill, A., Bralower, T. J., & Premoli-Silva, I. (2003). A Transient Rise in Tropical Sea Surface Temperature during the Paleocene-Eocene Thermal Maximum. *Science*, *302*(5650), 1551–1554. https://doi.org/10.1126/science.1090110

Zachos, J., Pagani, H., Sloan, L., Thomas, E., & Billups, K. (2001). Trends, rhythms, and aberrations in global climate 65 Ma to present. *Science*, *292*(5517), 686–693. https://doi.org/10.1126/science.1059412

Zhou, X., Thomas, E., Rickaby, R. E. M., Winguth, A. M. E., & Lu, Z. (2014). I/Ca evidence for upper ocean deoxygenation during the PETM. *Paleoceanography*, *29*(10), 964-975. https://doi.org/10.1002/2014pa002702

Zhou, X., Thomas, E., Winguth, A. M. E., Ridgwell, A., Scher, H., Hoogakker, B. A. A., Rickaby, R. E. M., & Lu, Z. (2016). Expanded oxygen minimum zones during the late Paleocene-early Eocene: Hints from multiproxy comparison and ocean modeling. *Paleoceanography*, *31*(12), 1532–1546. https://doi.org/10.1002/2016PA003020